Monthly Notices of the ROYAL ASTRONOMICAL SOCIETY

MNRAS **520,** 1371–1389 (2023) https://doi.org/10.1093/mnras/stac3815
Advance Access publication 2023 January 31

VST ATLAS galaxy cluster catalogue I: cluster detection and mass calibration

Behzad Ansarinejad ,[1,2]★ David Murphy,[3] Tom Shanks [1] and Nigel Metcalfe [1]

[1]*Centre for Extragalactic Astronomy, Department of Physics, Durham University, South Road, Durham DH1 3LE, UK*
[2]*School of Physics, University of Melbourne, Parkville, VIC 3010, Australia*
[3]*Institute of Astronomy, University of Cambridge, Madingley Road, Cambridge CB3 0HA, UK*

Accepted 2022 December 22. Received 2022 December 15; in original form 2022 July 8

ABSTRACT

Taking advantage of ∼4700 deg^2 optical coverage of the Southern sky offered by the VST ATLAS survey, we construct a new catalogue of photometrically selected galaxy groups and clusters using the ORCA cluster detection algorithm. The catalogue contains ∼22 000 detections with $N_{200} > 10$ and ∼9000 with $N_{200} > 20$. We estimate the photometric redshifts of the clusters using machine learning and find the redshift distribution of the sample to extend to $z \sim 0.7$, peaking at $z \sim 0.25$. We calibrate the ATLAS cluster mass-richness scaling relation using masses from the MCXC, Planck, ACT DR5, and SDSS redMaPPer cluster samples. We estimate the ATLAS sample to be > 95 per cent complete and > 85 per cent pure at $z < 0.35$ and in the $M_{200\mathrm{m}}>1 \times 10^{14}h^{-1}\,\mathrm{M}_{\odot}$ mass range. At $z < 0.35$, we also find the ATLAS sample to be more complete than redMaPPer, recovering a ∼ 40 per cent higher fraction of Abell clusters. This higher sample completeness places the amplitude of the $z < 0.35$ ATLAS cluster mass function closer to the predictions of a ΛCDM model with parameters based on the Planck CMB analyses, compared to the mass functions of the other cluster samples. However, strong tensions between the observed ATLAS mass functions and models remain. We shall present a detailed cosmological analysis of the ATLAS cluster mass functions in paper II. In the future, optical counterparts to X-ray-detected *eROSITA* clusters can be identified using the ATLAS sample. The catalogue is also well suited for auxiliary spectroscopic target selection in 4MOST. The ATLAS cluster catalogue is publicly available at http://astro.dur.ac.uk/cosmology/vstatlas/cluster_catalogue/.

Key words: catalogues – galaxies: clusters: general – cosmological parameters – large-scale structure of Universe – cosmology: observations.

1 INTRODUCTION

In the context of hierarchical structure formation, primordial peaks in the density field of the early Universe collapse and merge, leading to the incremental formation of gravitationally bound haloes of increasing mass (e.g. Peebles 1980). Galaxy clusters are the largest of these gravitationally bound structures in the Universe, occupying the extreme tail of the halo mass function. As a result, the evolution of galaxy cluster abundance with mass and redshift is extremely sensitive to variations in cosmological parameters. Precise observations of large numbers of clusters over a wide range of masses and redshifts can therefore provide powerful cosmological constraints (see reviews by Allen, Evrard & Mantz 2011; Weinberg et al. 2013). In the context of the ΛCDM model, the study of galaxy clusters can place independent constraints on Ω_m, the matter density parameter (Evrard 1997; Schuecker et al. 2003), Ω_Λ, the dark energy density parameter, and ω, the dark energy equation of state parameter (Morandi & Sun 2016), as well as σ_8, the normalization of the matter power spectrum on the scale of $8\,h^{-1}$Mpc (e.g. White, Efstathiou & Frenk 1993). Furthermore, extensions to ΛCDM such as massive neutrinos can be investigated via the study of galaxy cluster number counts (Costanzi et al. 2013; Roncarelli, Carbone & Moscardini 2015), while non-standard modified gravity models can be constrained via the study of cluster properties (Brownstein 2009; Llinares & Mota 2013; Planck Collaboration XIII 2016a; Bocquet et al. 2019). Galaxy clusters and groups also provide useful tools in studying galaxy evolution in extreme environments and their physical properties could aid our understanding of structure formation, providing vital information on collapse of dark matter and evolution of baryons in dark matter potentials (see reviews by Rosati, Borgani & Norman 2002; Voit 2005; and Kravtsov & Borgani 2012).

In the optical regime, the Sloan Digital Sky Survey (SDSS; York et al. 2000) was one of the first wide-field surveys covering ∼10 000 deg^2 of the sky, which formed the basis of the MAXBCG (Koester et al. 2007) and redMaPPer (Rykoff et al. 2014) cluster catalogues. The VST ATLAS survey (Shanks et al. 2015), which is the basis of this work, later provided coverage of ∼4700 deg^2 over the southern sky to similar depths as SDSS, but with superior seeing. Other notable recent and upcoming photometric surveys include Dark Energy Survey (DES; The Dark Energy Survey Collaboration 2005; Rykoff et al. 2016), Pan-STARRS (Kaiser et al. 2002; Ebeling et al. 2013), the Kilo-Degree Survey (KiDS; de Jong et al. 2013; Radovich et al. 2017), the Hyper-Suprime Camera (HSC; Aihara et al. 2018), and the Legacy Survey of Space and Time (LSST; LSST Dark Energy

★ E-mail: behzad.ansarinejad@unimelb.edu.au

Science Collaboration 2012), 4-metre Multi-Object Spectroscopic Telescope (4MOST; de Jong et al. 2019) and *Euclid* (Laureijs et al. 2011), providing enormous quantities of data upon which the search for clusters of galaxies has and will be based.

In the absence of spectroscopic redshifts, galaxy redshifts can be estimated photometrically based on techniques such as SED template fitting (e.g. HYPERZ; Bolzonella, Miralles & Pelló 2000), using Bayesian probabilistic methods (e.g. BPZ; Benítez 2011) or via machine learning approaches utilizing artificial neural networks or boosted decision trees (e.g. ANNZ2; Sadeh, Abdalla & Lahav 2016). Due to their large uncertainties, however, photometric redshifts alone are not sufficient for accurate identification of galaxy clusters via 3D reconstruction of the distribution of galaxies. A commonly adopted method of detecting galaxy clusters in the optical regime is taking advantage of the cluster *red sequence* (Baum 1959; Bower, Lucey & Ellis 1992; Gladders & Yee 2000). The red sequence refers to the tight correlation followed by the cluster galaxies in the colour–magnitude space, this feature arises due to galaxy clusters mostly containing early-type elliptical and lenticular galaxies which consist of passively evolving stellar populations giving rise to strong metal absorption lines at wavelengths bluewards of 4000 Å. As a result, the majority of cluster members appear red in colour and occupy a narrow ridge in the colour–magnitude space, when viewed through broad-band photometric filters that straddle the 4000 Å break. In this way cluster galaxies can be isolated from active, star-forming field galaxies. Algorithms utilizing the red sequence for cluster detection include Koester et al. (2007); Gladders et al. (2007); Thanjavur, Willis & Crampton (2009); Hao et al. (2010); Rykoff et al. (2014) as well as The Overdense Red-sequence Cluster Algorithm (ORCA; Murphy, Geach & Bower 2012) used in this work.

Galaxy clusters have also been detected in X-ray by exploiting the radiation due to thermal bremsstrahlung and line emission from the Inter Cluster Medium (Cavaliere & Fusco-Femiano 1976; Allen, Schmidt & Fabian 2002). In this work, we compare our optically detected cluster catalogue with the 'MCXC: a meta-catalogue of X-ray detected clusters of galaxies' (Piffaretti et al. 2011) which contains ∼1700 X-ray detected clusters. In the near future, an ongoing all-sky X-ray survey *eROSITA* (Merloni et al. 2012) with the aim of detecting ∼100 000 galaxy clusters out to $z > 1$ will significantly increase the cluster sample size in the X-ray regime. The cluster catalogue introduced in this work will provide a valuable resource which could be used to better characterize the selection function of the *eROSITA* cluster in terms of sample completeness and purity.

inverse-Compton scattering due to interaction with high energy electrons in the ICM provides a boost in energy to the cosmic microwave background (CMB) photons passing through clusters, making them detectable via a phenomenon known as the Sunyaev–Zel'dovich (SZ) effect (Sunyaev & Zeldovich 1980). With the benefit of a detection signature that is essentially redshift independent, the SZ effect offers a new window on the cluster population providing a nearly mass-limited sample at high redshifts, where cluster abundance can place sensitive constraints on cosmological parameters (Carlstrom, Holder & Reese 2002; Planck Collaboration XVI 2014b). In recent years, several SZ surveys have been undertaken with South Pole Telescope (SPT; Carlstrom et al. 2011) survey, the Atacama Cosmology Telescope (ACT; Fowler et al. 2007), and Planck (Tauber et al. 2010), providing the first SZ-selected cluster samples (Menanteau et al. 2010; Vanderlinde et al. 2010; Planck Collaboration VIII 2011; Hasselfield et al. 2013; Reichardt et al. 2013). In this work, we also draw a comparison between our cluster catalogue and the second Planck catalogue of SZ sources (henceforth Planck SZ; Planck Collaboration XIII 2016c), which contains 1653 detections, out of which 1203 are confirmed clusters based on identification of counterparts in external data sets. Similarly, we compare the ATLAS cluster catalogue with SZ detections from the ACT DR5 sample (Hilton et al. 2021), which has a large overlap with part of ATLAS in the Southern Galactic Cap (SGC). The ACT DR5 sample contains over 4000 cluster detections in a survey area of 13 168 deg^2, probing lower cluster masses than the Planck SZ sample.

We then present a calibration of the ATLAS cluster mass-richness scaling relation using cluster masses from the MCXC, ACT DR5, Planck, and SDSS redMaPPer samples. Our final aim in this work is to compare the observed mass function of the ATLAS cluster catalogue to theoretical predictions of ΛCDM based on the Tinker et al. (2008) model and other cluster samples. We choose the Tinker et al. (2008) model due to its common use in literature for cosmological analyses of various cluster samples over the past decade. (see e.g. Vikhlinin et al. 2009; Allen et al. 2011; Bleem et al. 2015; Planck Collaboration XIII 2016b; Bocquet et al. 2019; Abbott et al. 2020). We perform this comparison in five redshift bins covering the range $0.05 < z < 0.55$ in order to examine the evolution of the cluster mass functions.

The layout of this paper is as follows: In Section 2 we describe the VST ATLAS galaxy input catalogue. Then in Section 3 we present a brief description of the ORCA algorithm, as well as a description of our machine learning approach to obtaining photometric redshifts for our clusters. We also present a description of our cluster richness and mass estimation. In Section 4, we present the ATLAS cluster catalogue and compare our results with external multiwavelength cluster samples, providing estimates of the completeness and purity of the ATLAS cluster catalogue. This is followed by a comparison of the observed cluster mass functions of the ATLAS, redMaPPer, Planck, and ACT DR5 samples, versus theoretical predictions. Finally, we conclude by summarizing the cosmological implications in Section 5. Unless otherwise specified, we assume a Planck Collaboration XIII (2016a) ΛCDM cosmology with $H_0 = 67.74$, $\Omega_\Lambda = 0.6911$, $\Omega_m = 0.3089$, $\sigma_8 = 0.8159$, present all magnitudes in the AB system and define our cluster masses as $M_{200\mathrm{m}}$ which is the mass enclosed in a halo with a density 200 × the mean matter density of the Universe.

2 DATA SET

The VST ATLAS (Shanks et al. 2015) is an European Southern Observatory (ESO) public survey of the southern sky, designed to provide optical imaging in *ugriz* bands to similar depths as SDSS in the north. The data are taken using the Very Large Telescope Survey Telescope (VST; Schipani et al. 2012) a 2.61-m telescope with a 1 deg^2 field of view located at the Paranal observatory. The total survey area consists of 4711 deg^2, with 2087 deg^2 in the Northern Galactic Cap (NGC) and 2624 deg^2 in the Southern Galactic Cap (SGC). The ATLAS coverage area is overlapped by the DES (The Dark Energy Survey Collaboration 2005), DESI (DESI Collaboration 2016), KiDS (de Jong et al. 2013), and *eROSITA* (Merloni et al. 2012) surveys. In the future, the 4MOST (de Jong et al. 2019), *Euclid* (Laureijs et al. 2011) and LSST (LSST Dark Energy Science Collaboration 2012) surveys will also provide multiwavelength imaging and spectroscopic coverage of the VST ATLAS survey area.

Based on the ATLAS DR4 data, we produce a band-merged *griz* catalogue using a pipeline developed with the 'Starlink Tables Infrastructure Library Tool Set' (STILTS; Taylor 2006) framework. During band-merging, we include all objects with detections in a minimum of two bands. In this work, we utilize the VST ATLAS aperture magnitudes provided by the Cambridge Astronomical Survey Unit (CASU)[1] for obtaining galaxy colours while relying on the CASU Kron pseudo-total magnitude for imposing magnitude limits on our galaxy samples. The ATLAS Kron magnitudes are measured using circular apertures of 2 × the Kron radius, with the definition of the Kron radius given by Bertin & Arnouts (1996). The use of aperture magnitudes to measure galaxy colours was motivated by the inspection of the red-sequence of rich, spectroscopically confirmed Abell clusters, as well as comparison of galaxy colours between ATLAS Kron and aperture magnitudes and SDSS model magnitudes in a ∼200 deg^2 overlap area between the two surveys. These tests showed that aperture magnitudes have a lower level scatter than Kron around the red-sequence and when compared to SDSS. On the other hand, comparison between ATLAS and SDSS shows that Kron magnitudes provide a more reliable measure of the galaxies' total magnitudes compared to aperture magnitudes, which could miss a larger fraction of the galaxy flux (see also Shanks et al. 2015). We denote aperture magnitudes corresponding to the ATLAS `Aperture flux 5` using the subscript 'A5'. This aperture has a radius of 2 arcsec and we apply the associated aperture correction labelled as `APCOR` in the CASU catalogue. For g, r, i, and z bands, the mean values of `APCOR5` are 0.12, 0.12, 0.11, and 0.12 mag. Although these aperture corrections are derived for stars, they also provide a first-order seeing correction for faint galaxies. Where Kron pseudo-total magnitudes are used, we correct these to total magnitude for galaxies by applying a −0.15 mag offset. This value is chosen based on an empirical comparison of the ATLAS Kron and SDSS model magnitudes for galaxies in an overlap area between the two surveys as shown by Shanks et al. (2015). We then correct all magnitudes for Galactic dust extinction $A_x = C_x E(B - V)$, with x representing a filter ($griz$), taking the SDSS C_x values presented in Schneider et al. (2007) (3.793, 2.751, 2.086, and 1.479 for $griz$, respectively) and using the Planck $E(B - V)$ map (Planck Collaboration XVI 2014a).

In order to isolate galaxies from stars in the ATLAS data, we use the default morphological classifications supplied in CASU catalogues, a description of which can be found in González-Solares et al. (2008). Reflections from bright stars in the VST ATLAS data could lead to the formation of circular haloes which in some cases can be misidentified as multiple extended sources and misclassified as galaxies by the CASU source detection algorithm. To overcome this, we mask circular regions around these bright stars based on cross-matching the input catalogue to the Tycho-2 Catalogue of the 2.5 million brightest stars (Høg et al. 2000). The Tycho bright stars are masked with radii varying according to their V-band magnitudes. For this purpose we choose the following radii based on visual inspection of stars with various magnitudes: $V < 8$: 340 arcsec; $8 < V < 9$: 80 arcsec; $9 < V < 10$: 45 arcsec; $10 < V < 11$: 30 arcsec; $V > 11$: 20 arcsec. However, depending on the position of the star on the CCD chip, in some cases the halo can be off-centred from the stars. The remaining stellar haloes and other major remaining artefacts such as nearby galaxies or satellite trails are manually removed by performing a visual inspection of the data.

The input catalogue given to ORCA for cluster detection consists of objects detected in two adjacent bands (i.e. $g - r$, $r - i$ or $i - z$ which are used for cluster red-sequence detection). We also require objects to be classified as galaxies in a minimum of two bands. Here, we only require objects to be classified as galaxies in two bands as demanding a galaxy classification in all bands was deemed too strict, resulting in a ∼ 10 per cent decrease in the overall sample size. The slight increase in stellar contamination introduced in this approach is unlikely to be a problem in our cluster detection, due to ORCA's reliance on the red sequence in selecting cluster members (see Section 3.1). We do not include the u-band due to its shallow depth and the fact that the incompleteness of u-band observations at the time of conducting this work would result in large gaps across the survey area.

As the VST ATLAS survey observations are conducted in 17 deg^2 blocks at constant Declination, taking data in a single band at a time, nightly variations in seeing, sky brightness and other observing conditions can result in slight variations in survey depth across different concatenations. After band merging, these slight fluctuations in object densities in some concatenations could result in artificial inhomogeneities across the sky. Consequently, we select magnitude limits of $g_{\mathrm{Kron}} < 22.0$; $r_{\mathrm{Kron}} < 21.6$; $i_{\mathrm{Kron}} < 21.1$; $z_{\mathrm{Kron}} < 19.9$ as a compromise between increasing the survey depth and increasing homogeneity between concatenations. The final input catalogues contain ∼8740 000 galaxies in the SGC and ∼7825 000 in the NGC of the survey.

3 METHODOLOGY

3.1 ORCA: The cluster detection algorithm

A detailed description of the 'Overdense Red-sequence Cluster Algorithm' (ORCA) which is used to create the ATLAS cluster catalogue can be found in Murphy et al. (2012). The algorithm detects the red sequence in pairs of adjacent bands or colours (in our case $g - r$, $r - i$, or $i - z$). In the first stage, the algorithm applies a selection function to the input catalogue in the form of narrow slices in the colour–magnitude space. This photometric filtering separates galaxies within a specific redshift range from foreground and background objects, broadly isolating the cluster galaxies via the 4000 Å break. By detecting clusters in two colours concurrently, foreground and background contamination can be significantly reduced, as galaxies follow unique tracks in different colour-redshift spaces. During this stage, the red sequence is isolated across a range of redshifts through modifications of the colour slice in successive runs of the algorithm, systematically scanning the entire photometric space.

Upon the application of photometric filtering, the algorithm estimates the surface density of the remaining galaxies by calculating the Voronoi diagram of their projected distribution on the sky. The Voronoi cells are then separated into overdense and underdense cells based on a user-specified probability threshold (P_{thresh}), related to how likely they are to belong to a random distribution (for more details, see Section 3.4 of Murphy et al. 2012). Finally using the Friend-of-Friends technique, the algorithm connects adjacent overdense cells until the density of the whole system falls below a user-defined critical density ($\sum_{\mathrm{crit}}$). At this stage, if the system has at least N_{gals} linked galaxies (in this case we set $N_{\mathrm{gals}} = 5$), it is defined as a cluster.

We optimize the P_{thresh} and $\sum_{\mathrm{crit}}$ parameters for performance on VST ATLAS based on multiple runs of the ORCA algorithm on a ∼300 deg^2 area and assessing its performance based on recovering the Abell, MCXC, redMaPPer, and Planck SZ clusters in this region. We then set $\sum_{\mathrm{crit}} = 2.5\bar{\sum}$ (where $\bar{\sum}$ is the mean galaxy density), and $P_{\mathrm{thresh}} = 0.0125$, using the default for other adjustable parameters of the algorithm as these do not have a major effect on improving the results. As the adjustment to the colour slice is, by design, less

[1] http://casu.ast.cam.ac.uk/surveys-projects/vst/technical/catalogue-generation

Table 1. Details of the samples used in our photometric redshift training. Here the redshift coverage, the mean redshift of the samples, and the number of galaxies which corresponds to the number of objects with redshifts identified as ATLAS cluster members by the ORCA algorithm.

Sample	Redshift coverage	$\bar{z}$	Number of galaxies	Reference
2dFGRS	$0.00 < z < 0.30$	0.13	9426	Colless et al. (2003)
SDSS DR12	$0.05 < z < 0.35$	0.15	5260	Alam et al. (2015)
GAMA G23	$0.05 < z < 0.50$	0.21	3008	Liske et al. (2015)
Primus	$0.05 < z < 0.60$	0.24	177	Cool et al. (2013)
2dFLenS	$0.05 < z < 0.75$	0.26	2717	Wolf et al. (2017)
BOSS LOWZ	$0.05 < z < 0.45$	0.26	375	Dawson et al. (2013)
BOSS CMASS	$0.40 < z < 0.75$	0.52	141	Dawson et al. (2013)

than the width of the red sequence, the same cluster can be identified multiple times in successive runs of the algorithm.

3.2 ANNZ2: Photometric redshift estimation

We make use of the publicly available ANNZ2[2] (Sadeh et al. 2016) algorithm in order to obtain photometric redshift estimates for the VST ATLAS cluster members. For this purpose, we simultaneously make use of a combination of two machine learning methods offered by the algorithm; Artificial Neural Networks (ANNs) and Boosted Decision Trees (BDTs). After performing various tests, this approach was shown to produce the best RMS scatter in comparison to using ANNs or BDTs alone. Here the RMS error is given by:

$$\sigma_{\Delta z/(1+z)} \equiv \sqrt{\frac{1}{n_{\rm gals}} \sum_{\rm gals} \left(\frac{z_{\rm photo} - z_{\rm spec}}{1 + z_{\rm spec}} \right)^2}, \qquad (1)$$

where $n_{\rm gals}$ is the number of galaxies in the training set and $z_{\rm photo}$ and $z_{\rm spec}$ are estimated photometric and measured spectroscopic redshifts of these galaxies, respectively.

To estimate photometric redshifts using machine learning, we are required to provide the algorithm with a training sample of galaxies with measured redshifts, which overlap the VST ATLAS survey area. For this purpose, we make use a total of 21 114 galaxies with redshifts obtained from various surveys as detailed in Table 1. In cases where the same objects have redshifts provided by more than one survey, we keep the redshift with the smaller uncertainty. Fig. 1 shows the redshift distribution of the galaxies included in the training set used in our photometric redshift estimation.

In order to improve our photometric redshift training, in addition to the ATLAS *griz* bands, we add the W1 and W2 magnitudes from the ‘unblurred coadds of the *WISE* imaging’ catalogue (unWISE; Schlafly, Meisner & Green 2019).[3] Here we use a 2 arcsec radius to match ATLAS and unWISE sources and we correct for Galactic dust extinction in W1 and W2 bands by subtracting $0.18 \times E(B - V)$ and $0.16 \times E(B - V)$ from the W1 and W2 magnitudes, respectively. These $E(B - V)$ values are taken from the same Planck dust map (Planck Collaboration XVI 2014b) used to correct the ATLAS magnitudes for Galactic dust extinction and the 0.18 and 0.16 coefficients are taken from Yuan, Liu & Xiang (2013).

Finally, we calculate the weighted mean photometric redshift of our clusters using: $\bar{z} = (\sum z_{\rm i}/\sigma_{\rm i}^2)/(\sum 1/\sigma_{\rm i}^2)$, where $z_{\rm i}$ and $\sigma_{\rm i}$ are the photometric redshift and photometric redshift uncertainty of the i-th cluster member. The uncertainty on the cluster redshift is then given by the standard error on the mean, and we verify the uncertainty using the Jackknife technique.

[2] https://github.com/IftachSadeh/ANNZ

[3] We note that despite the 6 arcsec *WISE* PSF, thanks to the improved modelling of the blended sources in the unWISE catalogue, the addition of W1 and W2 information to our machine learning training still proved useful in improving our photo-z RMS scatter.

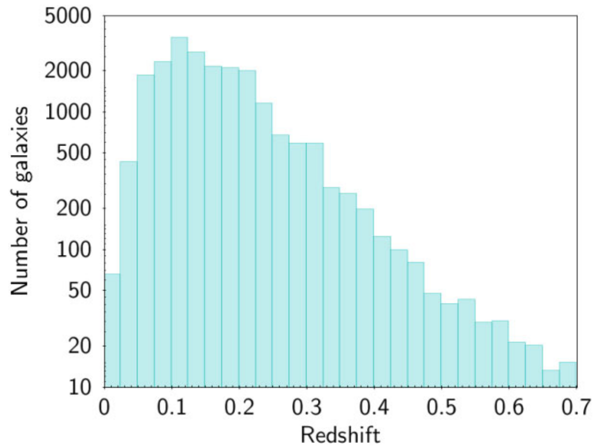

Figure 1. The redshift distribution of the training sample used to estimate the photometric redshifts of the ATLAS galaxy cluster members by ANNZ2.

3.3 Cluster catalogue post-processing

As discussed in 3.6 of Murphy et al. (2012), multiple detections of the same cluster found in different colour–magnitude spaces are merged together by ORCA based on five tests of ‘cluster similarity’. These criteria are based on the similarity of the clusters’ red-sequence, the extent of spatial overlap and the number of common galaxies between the two detections.

In this work, we utilize our photometric redshifts to further merge overlapping cluster detections that are likely to belong to the same system based on the following criteria:

(i) **Spatial overlap:** A cluster centre lies within the cluster radius of a nearby cluster. Here, the cluster centre is defined as the mean RA and Dec of its cluster member and cluster radius is defined as the angular separation between the furthest cluster member and the cluster centre. In addition, we require at least one of the criteria below to be satisfied in order for overlapping detections to be considered as part of the same system.

(ii) **Photometric redshift overlap:** The error weighted mean cluster photometric redshift lies within one standard error of another spatially overlapping cluster.

(iii) **Red-sequence overlap:** The mean colour of a cluster’s members (in either $g - r$, $r - i$, or $i - z$) is within one standard error of another spatially overlapping cluster’s mean colour.

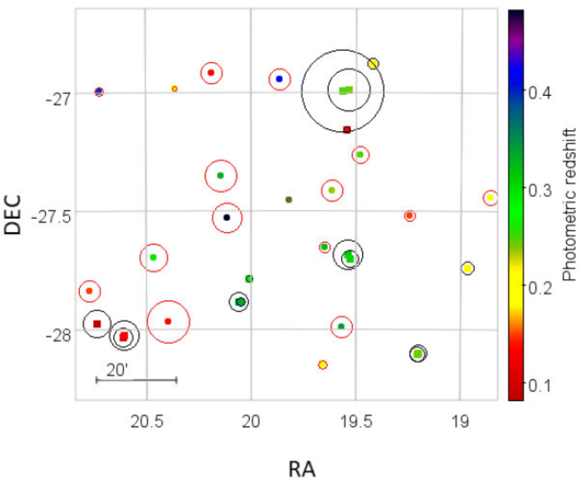

Figure 2. The outcome of merging overlapping clusters based on spatial and photometric redshift, or red-sequence overlap. Here, circles show the corresponding cluster radii used to identify spatially overlapping clusters, with the black circles marking clusters that are merged.

Requiring the combination of spatial overlap, with either photometric redshift or red-sequence overlap results in the merging of 9 per cent of the clusters in the catalogue. Fig. 2 shows an example of merged overlapping clusters based on the above criteria.

3.4 Cluster richness (N_{200})

In order to provide an estimate of cluster richness, we first count the number of cluster galaxies within a 1 h^{-1} Mpc aperture of the cluster centre, $N_{\rm 1Mpc}$, which in the i-band, are fainter than the Brightest Cluster Galaxy (BCG), and brighter than $0.4L_*$. Here L_* is the characteristic luminosity in the Schechter luminosity function, and following Reyes et al. (2008), we take the $z = 0.1$, i-band value of $L_* = 2.08 \times 10^{10} h^{-2}\,{\rm L}_\odot$. To calculate the K-corrections, we make use of the 'K-corrections calculator' Python algorithm[4], which is based on the procedure described in Chilingarian, Melchior & Zolotukhin (2010).

Once the values of $N_{\rm 1Mpc}$ are determined, we calculate the cluster radius R_{200}, defined as the radius within which the cluster galaxy number density is $200\Omega_m^{-1}$ times the mean galaxy density of the present Universe. We calculate R_{200} (in units of h^{-1}Mpc) using an empirical relation presented by Hansen et al. (2005):

$$R_{200} = (0.142 \pm 0.004) N_{\rm 1Mpc}^{0.6\pm0.01}, \tag{2}$$

based on their analysis of the SDSS maxBCG clusters. R_{200} is in turn used to obtain the final cluster richness N_{200} which is calculated in the same way as $N_{\rm 1Mpc}$, but now using R_{200} as the aperture within which the cluster members are counted as opposed to the fixed aperture of 1 Mpc.

3.5 Scaling N_{200} by $n(z)$

Due to the magnitude limits of our data, our ability to detect fainter cluster members is reduced as a function of redshift, which could lead to an underestimation of our cluster N_{200} values at higher redshifts. In order to correct for the impact of the survey magnitude limits on our N_{200} and subsequent cluster mass ($M_{\rm 200m}$) estimation, we up-weight our N_{200} values by a theoretical galaxy $n(z)$ curve which gives the relative number of galaxies detectable as a function of redshift, given our $i < 21.1$ magnitude limit. This theoretical $n(z)$ is obtained based on a luminosity function which assumes a Schechter (1976) function, with the i-band, 'red' galaxy values of $\alpha = -0.46$ and the $z = 0.1$ value of $M^* - 5\log h = -20.63$ taken from table 3 of Loveday et al. (2012), k and evolution corrected (with a star-formation time-scale of $\tau = 2.5$ Gyr), using the Stellar population synthesis model of Bruzual & Charlot (2003).

Fig. 3(a) shows the cluster membership of our ORCA clusters (highlighting ORCA clusters matched to Planck, ACT DR5, MCXC, and Abell cluster samples) as a function of redshift. Here, we are also plotting the theoretical $n(z)$ described above, normalized to match our maximum value of $N_{\rm gal} = 220$ at $z = 0.1$. Also shown is a fitted curve to the theoretical $n(z)$ which is used to obtain the scaling factor, $C(\bar{z})$, applied to our N_{200} in the $z > 0.1$ redshift range, where the number of our cluster members begin to drop as a function of redshift. This scaling factor takes the form of:

$$C(\bar{z}) = 220/(571.7\bar{z}^2 - 819\bar{z} + 292.8), \tag{3}$$

i.e. the ratio of $N_{\rm gal} = 220$ to our normalized theoretical $n(z)$ at each redshift and is shown in Fig. 3(b) as a function of redshift.

In order to apply the $C(\bar{z})$ scaling to our N_{200} values, we first scale our $N_{\rm 1Mpc}$ values which are used to estimate the value of R_{200} for each cluster, thus ensuring our R_{200} values are not underestimated at higher redshifts. We then count the number of cluster galaxies within R_{200} and scale this number by the $C(\bar{z})$ to obtain the N_{200} values plotted in Fig. 4(a). In this manner, when estimating the richness of our clusters, we account for the increased likelihood of cluster galaxies remaining undetected with increasing redshift. The uncertainty on the scaled N_{200} is then given by propagation of the $\sqrt{n}$ error on N_{200} and the uncertainty on $C(\bar{z})$:

$$\sigma_{N_{200}} = 2200 \times \sqrt{\frac{4N_{200}^2(5717\bar{z} - 4095)^2\sigma_{\bar{z}}^2 + N_{200}(5717\bar{z}^2 - 8190\bar{z} + 2928)^2}{(5717\bar{z}^2 - 8190\bar{z} + 2928)^4}}. \tag{4}$$

Note that in the above equation the N_{200} values are not scaled by $C(\bar{z})$. For the remainder of this work, however, unless otherwise specified, our use of N_{200} refers to these $n(z)$ scaled N_{200} values.

We note that our cluster mass estimates and the resulting mass functions as presented in Sections 4.5 and 4.6 are not very sensitive to the chosen value of normalization and exact parameters of equation (3). This is because any systematic redshift-dependent offsets introduced during the $n(z)$ scaling is removed when we calibrate our cluster mass-richness scaling relation to cluster masses from external samples in the next Section.

3.6 ATLAS cluster mass-richness scaling relation

Using our N_{200} estimates from Section 3.4, along with the mean photometric redshifts of our clusters, $\bar{z}$, we provide cluster masses $M_{\rm 200m}$ (in units of $10^{14} h^{-1}{\rm M}_\odot$) based on the following scaling relation:

$$M_{\rm 200m} = \left(\frac{N_{200}}{20}\right)^{1.1} \times 3\bar{z}^{\,0.9} + 1. \tag{5}$$

[4] http://kcor.sai.msu.ru/getthecode/

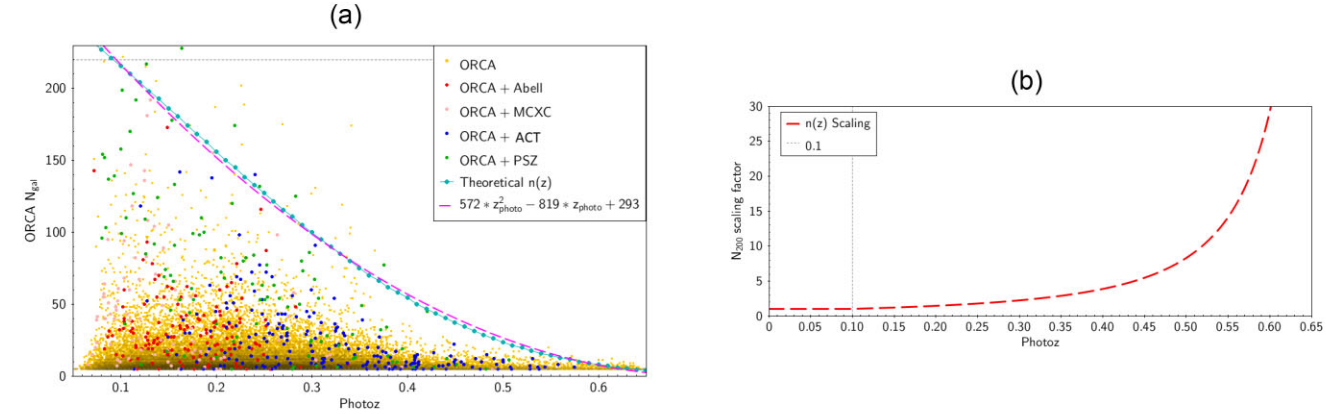

Figure 3. (a) ORCA cluster membership $N_{\rm gal}$ as a function of photometric redshift. We also highlight ORCA clusters with counterparts in Planck SZ, MCXC, ACT DR5, and Abell cluster catalogues. The best-fitting curve (dashed pink line), fitted to the normalized theoretical $n(z)$ described in Section 3.5 is used to determine the redshift dependent N_{200} scaling factor shown in panel (b).

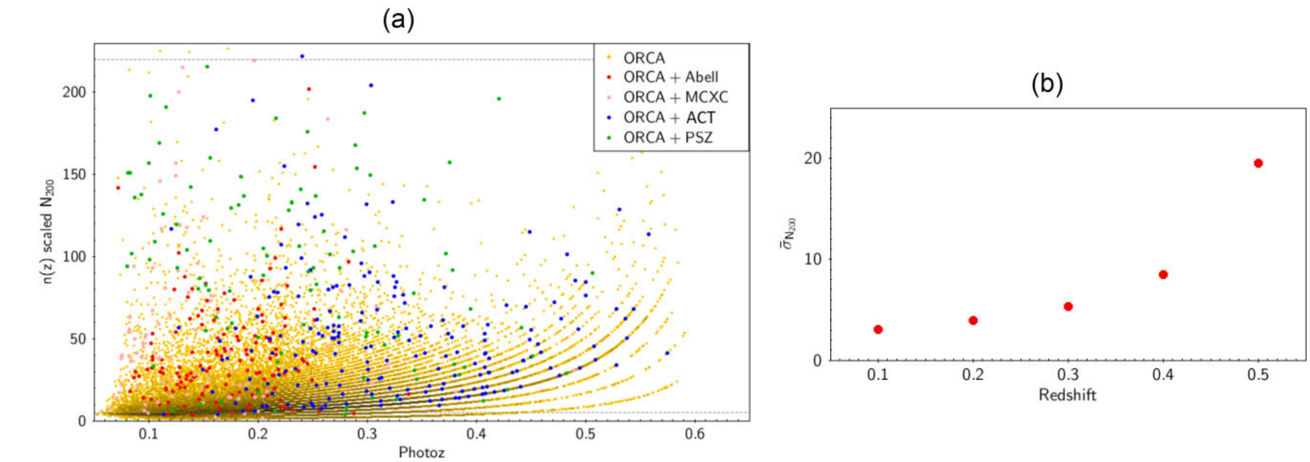

Figure 4. (a) $n(z)$ scaled N_{200} values as a function of photometric redshift. A comparison of this plot with Fig. 3(a) shows that this scaling has compensated for our tendency to underestimate cluster richness values with increasing redshift. For clarity, we do not show the error bars on the scaled N_{200} values in panel (a). However, in panel (b) we show the mean uncertainty on the scaled N_{200} values as a function of cluster photometric redshift.

The form and parameters of this relation are chosen based on comparison[5] of the resulting ATLAS cluster mass estimates to masses of 626 clusters from external samples. These include 218 ACT DR5 and 95 Planck SZ clusters, 185 SDSS redMaPPer clusters and 118 MCXC X-ray clusters. The error on our cluster masses are then approximated using:

$$\sigma_{M_{200}\mathrm{m}} = \sqrt{0.015\sigma^2_{N_{200}} N_{200}^{0.2} \bar{z}^{1.8} + \frac{0.01 N_{200}^{2.2} \sigma^2_{\bar{z}}}{\bar{z}^{0.2}}}, \qquad (6)$$

where $\sigma_{\bar{z}}$ and $\sigma_{N_{200}}$ are the uncertainties on $\bar{z}$ and N_{200}, respectively.

Fig. 5 shows the redshift and mass distribution of the clusters from these four samples. The combination of these samples provide a reasonable number of counterparts to ATLAS clusters across the redshift range of $0.05 < z < 0.55$ and the mass range of 10^{14}–$10^{15}\,\mathrm{M}_\odot$. To select the cluster counterparts, we use the ORCA cluster radius ($R_{\rm ORCA}$) as our matching radius for the ACT DR5, redMaPPer, MCXC, and Abell cluster catalogues, while using the Planck position uncertainty on the SZ cluster centre as the matching radius. Here, we calibrate the parameters in our cluster mass-richness scaling relation (equation 5) using all available cluster masses from these four samples simultaneously, to avoid biasing our masses towards the range of masses covered by the individual samples.

We obtain the masses of the redMaPPer clusters using the weak lensing calibrated mass-richness scaling relation of Simet et al. (2016), with $M_{200\mathrm{m}} = 10^{14.344}(\lambda/40)^{1.33}$. Here, $M_{200\mathrm{m}}$ is the M_{200} cluster mass with respect to the mean density of the Universe (in units of $10^{14}h^{-1}\,\mathrm{M}_\odot$) and λ is the richness of redMaPPer clusters as defined by Rykoff et al. (2014). Similarly, we use the $M_{200\mathrm{m}}$ cluster masses from the ACT DR5 catalogue. As the MCXC cluster masses are defined as M_{500}, we multiply these by a factor of 1.5 in order to remove the mean offset found between the MCXC M_{500} masses and the $M_{200\mathrm{m}}$ masses of their redMaPPer and ACT DR5 counterparts. We correct for the mean offset between the Planck SZ mass proxy values, $M_{\rm SZ}$, and the $M_{200\mathrm{m}}$ masses of their redMaPPer and ACT DR5 counterparts, by multiplying the Planck masses by a factor of 1.3. Once the Planck and MCXC masses are scaled to roughly correspond to $M_{200\mathrm{m}}$ masses, we use the masses from the four samples to obtain the ATLAS mass-richness scaling relation given by equation (5). In the case of the ACT DR5 and Planck SZ samples, we limit the sources to those with an SNR>5.

[5]The ATLAS mass-richness scaling relation is chosen to minimize the offset and scatter in Fig. 6(a).

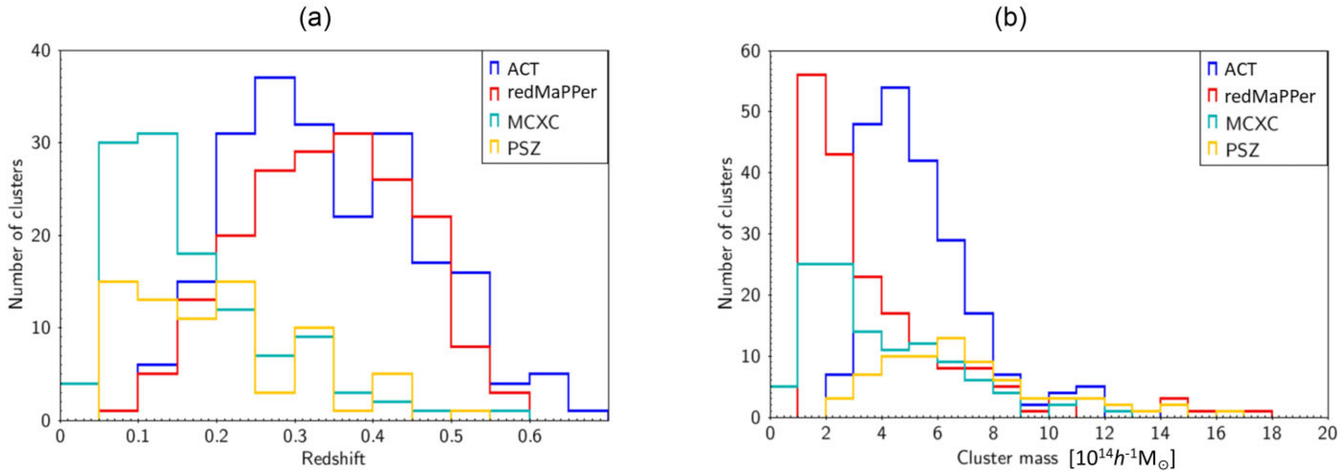

Figure 5. Redshift (a) and mass (b) distributions of the clusters from the ACT DR5, redMaPPer, MCXC, and Planck SZ cluster catalogues, used to calibrate the ATLAS cluster masses.

The ratio of our ORCA cluster masses to masses based on their counterparts from these four samples are shown in Fig. 6(a). Our cluster masses are calibrated on the basis of minimizing the mean offset and scatter in this plot as well as the mass ratio histogram shown in Fig. 6(b). The level of scatter found in the ratio of our richness-based cluster mass estimates to masses from external X-ray and SZ samples is comparable to that found when we compare the redMaPPer richness-based cluster masses to masses from these external samples.

The photometric redshift term in our ATLAS mass-richness scaling relation (equation 5) is added to remove a redshift-dependent offset found between our $M_{200\mathrm{m}}$ masses and the masses from the four external catalogues. This redshift dependence may be partially due to the presence of a slight systematic offset towards lower redshifts in our photometric redshift estimates in the $z > 0.35$ redshift range, which is likely caused by the relatively lower number of galaxies in our spectroscopic training set in this redshift range (see Figs 1, 8 and the discussion in Section 4.2). The presence of such systematic offset towards lower redshift will, in turn, result in a lower $n(z)$ scaling factor being applied to the high redshift cluster richness values, biasing our estimates of N_{200} and $M_{200\mathrm{m}}$ low.

In addition, although no evidence has been found to suggest cluster mass-to-light ratios (M/L) increase as a function of redshift (e.g. Lin et al. 2006; Muzzin et al. 2007; Soucail et al. 2015), the increase of cluster M/L as a function of cluster mass has been well established. Over a wide range of masses, various studies have found a ratio of $M/L \propto M^{\alpha}$, with α ranging from 0.2 to 0.4 (Girardi et al. 2002; Lin, Mohr & Stanford 2003; Rines et al. 2004; Popesso et al. 2007). Given that with increasing redshift (and in the $z > 0.3$ range in particular) due to the magnitude limits of our sample we are increasingly likely to miss smaller, lower mass clusters, with the same being true (to varying degrees) for the external cluster samples used in our mass calibrations[6], the increased fraction of higher mass clusters at higher redshifts could mean that our $N - M$ scaling relation which provided a good estimate of total cluster masses at lower redshifts, is underestimating the mass of our high redshift population which tend to have higher M/L ratios due to their higher mass.

[6]This is due to the flux limit of the redMaPPer and MCXC samples, and for Planck and ACT DR5, due to the SZ lower limit of cluster mass observability.

4 RESULTS AND DISCUSSION

4.1 The VST ATLAS cluster catalogue

Table 2 provides a description of the ATLAS catalogue columns, detailing the various properties of clusters including redshift, richness, cluster radius, and cluster mass. For each catalogue column, we provide the column title given in the catalogue, the corresponding symbol as used in the text of this work, followed by the units and a description of the values in each column. Table 3 provides a description of the columns in the ATLAS cluster members catalogues providing unique identifiers, coordinates, and photometric redshifts of each cluster galaxy.

4.2 Photometric redshifts

Following the procedure described in Section 3.2, we use ANNZ2 to obtain photo-z estimates for our cluster galaxies with an RMS scatter of ∼0.024 (see Fig. 7a), upon removing the outliers given by $((z_{\mathrm{photo}} - z_{\mathrm{spec}})/(1 + z_{\mathrm{spec}})) > 0.15$. Inclusion of outliers results in an RMS of ∼0.026. The error-weighted mean photometric redshift of the full ATLAS sample containing ∼40 000 ORCA detections with $N_{200} \geq 5$, as well as ∼22 000 clusters with $N_{200} > 10$ and 9000 clusters with $N_{200} > 20$ are shown in Fig. 7(b). Here, the peaks of the distributions lie at $z \sim 0.25$ and clusters are detected up to $z \sim 0.7$ (or $z \sim 0.6$ for clusters with $N_{200} > 20$).

Fig. 7(c) shows the distribution of the Standard error on the mean cluster redshift peaking at ∼0.02 for the full sample, and ∼0.01 for clusters with $N_{200} > 20$. Finally, for the full sample, we show the uncertainty on the mean cluster photometric redshifts as a function of redshift in Fig. 7(d), finding a good agreement between the Jackknife and standard error estimates of the uncertainty.

In Fig. 8 we compare the photometric redshift of our ATLAS clusters with spectroscopic redshifts from their cluster counterparts from MCXC, SDSS redMaPPer, Planck, and ACT DR5 samples. Here the $>3\sigma$ outliers (based on mean cluster photo-z error of ∼0.03) are marked by the dotted lines and constitute ∼ 6 per cent of the sample. While we find a general agreement between the ATLAS photometric redshifts and the spectroscopic redshifts from external samples, we also note hints of systematics at $z > 0.3$ where our photometric redshifts appear more likely to be underestimated.

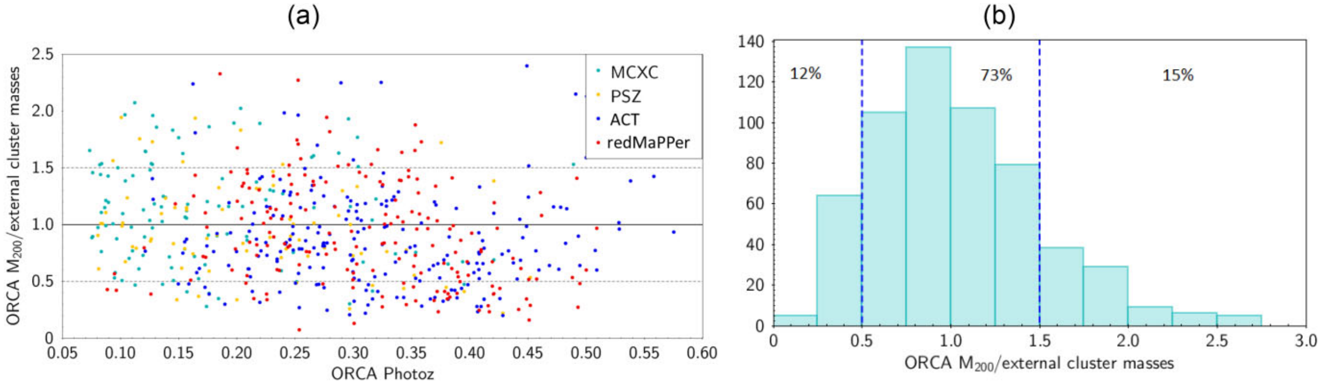

Figure 6. (a) The ratio of our ORCA cluster masses to masses of their cluster counterparts from external samples. The dotted lines show regions where our masses are in agreement with external masses within ±50 per cent. (b) Histogram showing the ratio of the ORCA cluster masses to external cluster masses shown in (a). Here, we mark the percentage of clusters with mass ratios below, above, and within the ±50 per cent region.

Table 2. A description of the columns of the ATLAS cluster catalogue. For each catalogue column, the symbols column of this table shows the corresponding symbol used in the text and figures of this paper.

Column	Symbol (units)	Description
ClusterID	–	A unique cluster identification number assigned to each cluster by the ORCA cluster detection algorithm.
RA	(Degrees J2000)	Right Ascension of the cluster centre (mean RA of cluster members).
DEC	(Degrees J2000)	Declination of the cluster centre (mean Dec of cluster members).
Photoz	$\bar{z}$	Error-weighted mean photometric redshift of the cluster.
Photoz_err	$\sigma_{\bar{z}}$	Standard Error on the mean cluster photometric redshift.
R_ORCA	$R_{\rm ORCA}$ (arcmin)	The projected radius of the ORCA cluster on the sky, defined as the angular separation between the cluster centre and the furthest cluster galaxy.
ORCA_Ngal	$N_{\rm gal}$	The number of cluster galaxies detected by ORCA.
N_1Mpc	$N_{1\,\rm Mpc}$	The number of cluster galaxies detected by ORCA within a radius of 1 h^{-1} Mpc from the centre of the cluster. This number is scaled by the theoretical $n(z)$ following equation (3).
R_200	R_{200} (arcmin)	The radius from the cluster centre within which the density is 200 × the mean density of the Universe (given by equation 2).
N_200	N_{200}	The number of cluster galaxies within a radius of R_{200} from the centre of the cluster. This number is scaled by the theoretical $n(z)$ following equation (3).
N_200_err	$\sigma_{N_{200}}$	The error on N_{200} given by equation (4).
M_200m	$M_{200\rm m}$ ($10^{14}h^{-1}$M$_\odot$)	The cluster mass enclosed within a radius of R_{200} from the centre of the cluster (given by equation 5). The cluster masses in our catalogue are measured with respect to the mean density of the Universe (often represented using the symbol $M_{200\,\rm m}$ in literature).
M_200m_err	$\sigma_{M_{200\rm m}}$ ($10^{14}h^{-1}$M$_\odot$)	The uncertainty on the $M_{200\rm m}$ cluster mass given by equation (6).

Table 3. A description of the columns of the ATLAS cluster members catalogue. For each catalogue column, the symbols column of this table shows the corresponding symbol used in the text and figures of this paper.

Column	Symbol (units)	Description
ClusterID	–	A unique cluster identification number assigned to each cluster by the ORCA cluster detection algorithm.
ObjID	–	A unique object identification number assigned to each cluster galaxy by the ORCA cluster detection algorithm.
RA	(Degrees J2000)	Right Ascension of the cluster member.
DEC	(Degrees J2000)	Declination of the cluster member.
g_mag	$g_{\rm A5}$	VST ATLAS g-band Aperture 5 (aperture radius of 2 arcsec) magnitude in the AB system.
r_mag	$r_{\rm A5}$	VST ATLAS r-band Aperture 5 (aperture radius of 2 arcsec) magnitude in the AB system.
i_mag	$i_{\rm A5}$	VST ATLAS i-band Aperture 5 (aperture radius of 2 arcsec) magnitude in the AB system.
z_mag	$z_{\rm A5}$	VST ATLAS z-band Aperture 5 (aperture radius of 2 arcsec) magnitude in the AB system.
W1_mag	W1	unWISE W1 magnitude in the AB system.
W2_mag	W2	unWISE W2 magnitude in the AB system.
Photoz	z	Cluster galaxy photometric redshift as determined by ANNZ2 machine learning algorithm (see Section 3.2).
Photoz_err	$\sigma(z)$	Error on cluster galaxy photometric redshift as determined by ANNZ2.

4.3 Mass and redshift completeness

Fig. 9(a) shows the fraction of clusters from the SDSS redMaPPer, ACT DR5, Planck, MCXC, and Abell catalogues overlapping the ATLAS coverage area that are detected in the ATLAS cluster catalogue. This provides a measure of the completeness of the ATLAS cluster sample as a function of redshift. In the case of the ACT DR5 and Planck samples, we limit the match to clusters with

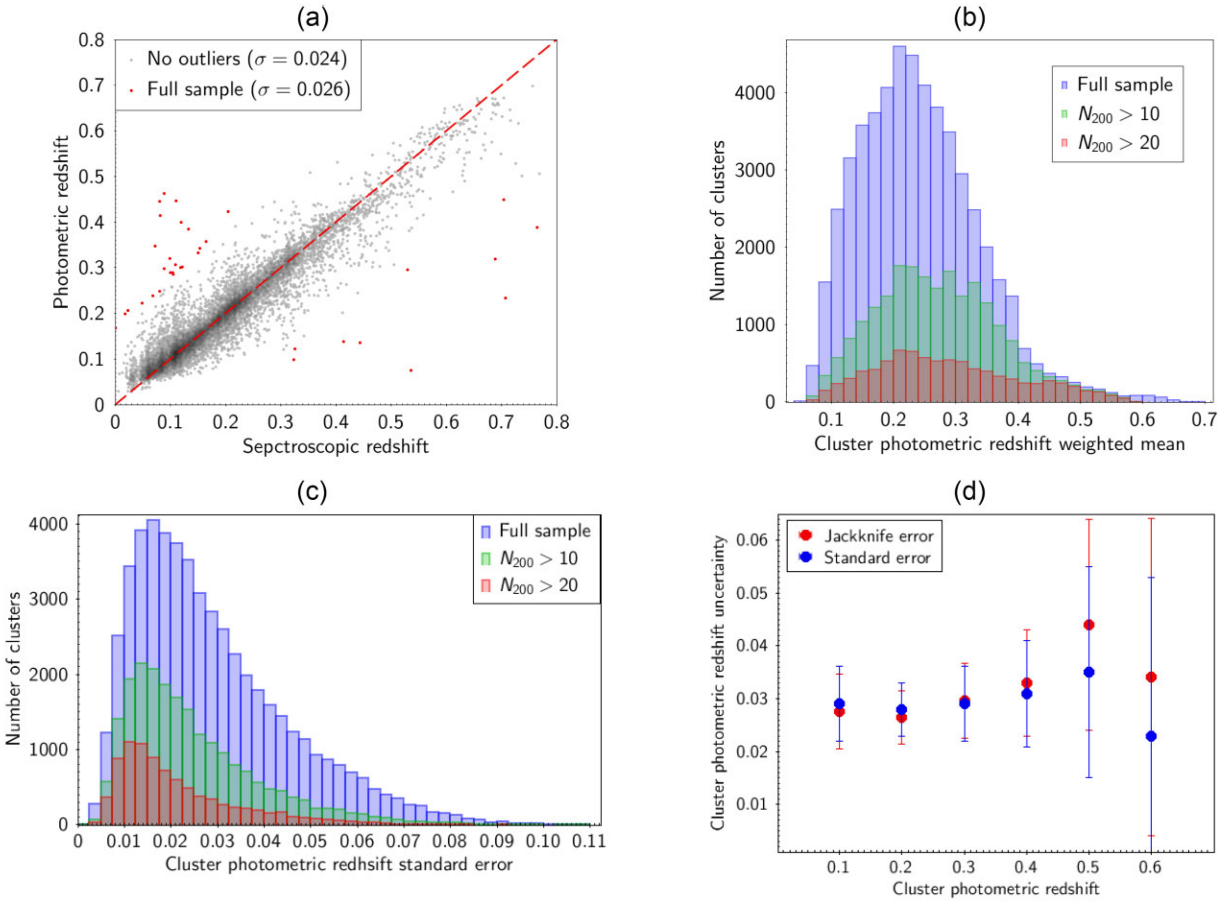

Figure 7. (a) Photometric versus spectroscopic redshift of the ORCA cluster members. The photometric redshifts are calculated following the procedure described in Section 3.2. Outliers (red) are defined as $(|z_{\rm photo} - z_{\rm spec}|/(1 + z_{\rm spec})) > 0.15$. (b) The distribution of the (error-weighted) mean photometric redshift of the VST ATLAS clusters, with the standard error on the cluster photometric redshift shown in panel (c). (d) A comparison of the Jackknife and standard error estimates of the cluster photometric redshift uncertainties shows a good agreement between the two estimates. Here the error bars represent the error in the error given by $1/\sqrt{2N-2}$, where N is the number of clusters in each redshift bin.

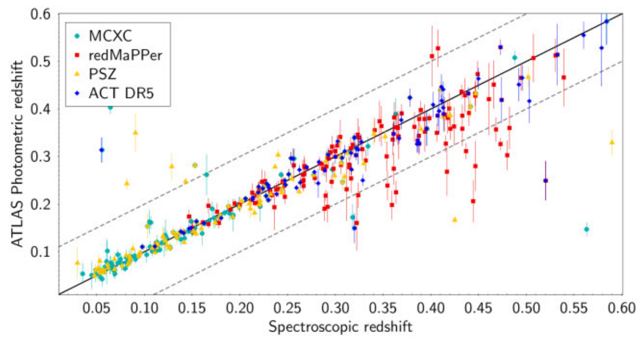

Figure 8. A comparison of our ATLAS cluster photometric redshifts to spectroscopic redshifts from the MCXC, SDSS redMaPPer, Planck, and ACT DR5 SZ cluster samples. The dotted lines mark the ± 0.1 ($\sim 3\sigma$) error region.

SZ detections with SNR > 5. In all cases, the cluster samples are limited to clusters with masses greater than $1 \times 10^{14} h^{-1}\,\mathrm{M}_{\odot}$, roughly corresponding to the lower mass limit of the ATLAS clusters. Fig. 9(b) shows the mean completeness of the ATLAS cluster samples as a function of redshift, where the sample is > 95 per cent complete in the range $z < 0.3$ and > 80 per cent complete up to $z = 0.4$. We note that the sharp fall in our completeness comparison to Planck at $z = 0.5$ is due to small number statistics of the Planck sample at this redshift range where we detect 3/7 Planck SZ clusters overlapping the ATLAS coverage area.

Fig. 10(a) shows the mass completeness of the ATLAS cluster catalogue by assessing the fraction of SDSS redMaPPer, ACT DR5, MCXC, and Planck clusters detected in the ATLAS sample as a function of cluster mass. Here, all samples are limited to the redshift range $0.1 < z < 0.3$ in order to ensure the mass completeness is not impacted by our reduced completeness at higher redshifts. Fig. 10(b) shows the mean cluster mass completeness of the ATLAS sample, with the sample being > 95 per cent complete across the full $1 \times 10^{14} - 1.5 \times 10^{15} h^{-1}\,\mathrm{M}_{\odot}$ mass range, with a near full recovery rate of external clusters for masses $> 5 \times 10^{14} h^{-1}\,\mathrm{M}_{\odot}$.

4.4 Comparison to redMaPPer

Fig.11 shows the number of ATLAS clusters as a function of cluster richness (N_{200}). A similar histogram showing the richness (λ) of the SDSS redMaPPer sample is also added for comparison. Although redMaPPer clusters with ($\lambda < 20$) are not available with the public release of the catalogue, it can be seen that both samples follow similar cluster richness distributions with thousands of clusters in bins of richness smaller than $\sim$40, hundreds in richness bins between $\sim$40 and 80, and tens of clusters in bins of richness ranging from

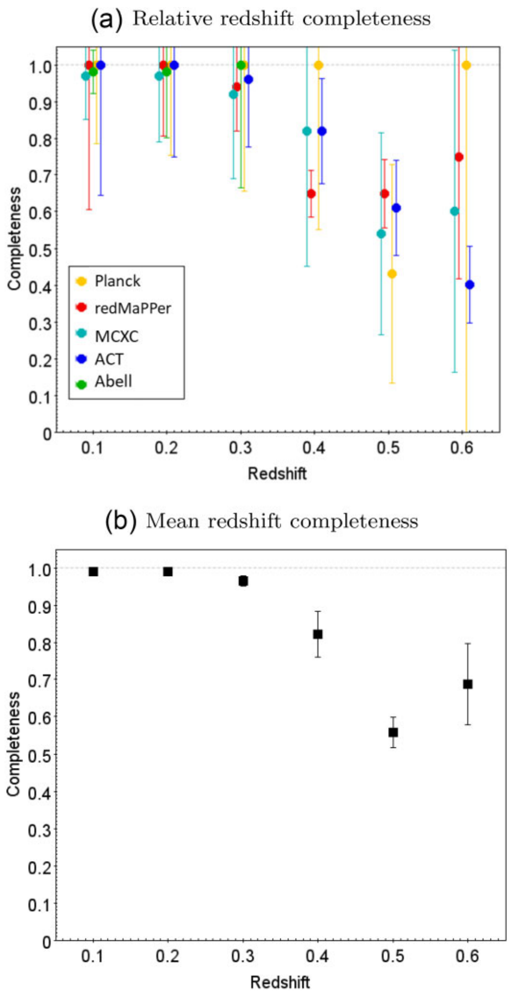

Figure 9. (a) The redshift completeness of the ATLAS cluster sample, based on the fraction of the recovered SDSS redMaPPer, ACT DR5, Planck, MCXC, and Abell clusters overlapping the ATLAS coverage area (see the text for selection and matching criteria). The error bars are given by the propagation of $\sqrt{n}$ error estimates and for clarity, the data points corresponding to different data sets have been slightly shifted along the x-axis. (b) The mean redshift completeness of the ATLAS clusters sample based on the comparison to external clusters in panel (a). Here, the error bars are given by the standard error on the mean.

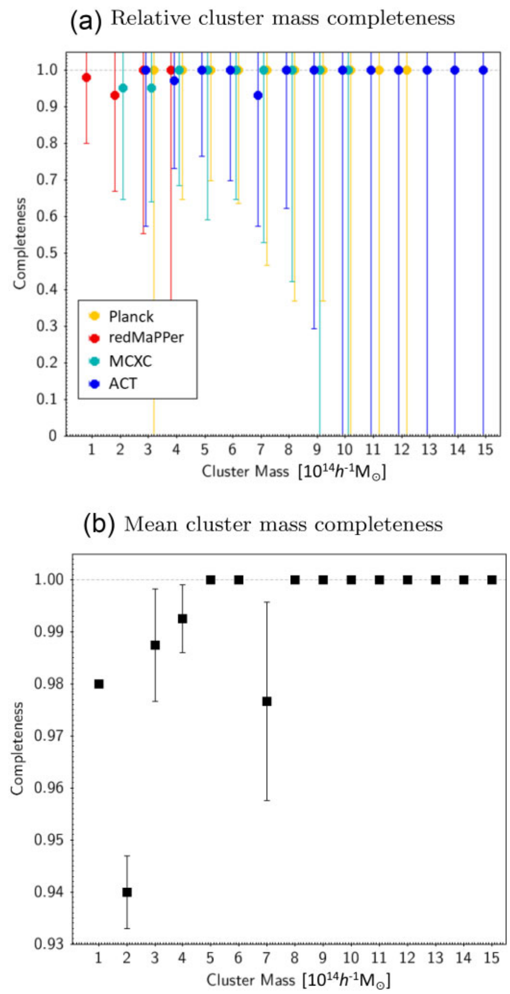

Figure 10. (a) The fraction of SDSS redMaPPer, ACT DR5, Planck, and MCXC clusters overlapping the ATLAS coverage area which are detected in the ATLAS cluster catalogue. This provides an estimate of the completeness of the ATLAS cluster sample as a function of mass. The error bars shown in this panel are given by the propagation of $\sqrt{n}$ error estimates and for clarity, the data points corresponding to different data sets have been slightly shifted along the x-axis. (b) The mean completeness of the ATLAS sample as a function of cluster mass, based on comparison to the samples shown in panel (a). Here, the error bars are given by the standard error on the mean.

~80–140. The ATLAS sample however contains a slightly larger number of richer clusters (~ 10 per cent), which is likely due to differences in cluster detection algorithms and the definitions of cluster richness between the two samples.

For the remainder of this section, we limit the ATLAS and redMaPPer samples to their mutual survey overlap area of ~200 deg^2, which constitutes ~ 4 per cent and ~ 2 per cent of the total ATLAS and SDSS survey areas, respectively. As the overlap area is situated at the edge of both surveys, we remove any cluster that lies within 5 arcmin of the survey boundaries. We highlight that given the limited overlap area, one should keep in mind that the comparisons in this section may not be representative of the complete cluster samples. In addition, unless otherwise specified, we limit the cluster samples to the $M_{200\mathrm{m}} > 3 \times 10^{14} h^{-1}\,\mathrm{M}_\odot$ mass range in the comparisons performed in this section.

In Fig. 12, we show a comparison of the ATLAS, redMaPPer, Abell, and ACT DR5 cluster catalogues in the ATLAS/SDSS survey overlap areas. For reasons that we will explore in more detail later, in

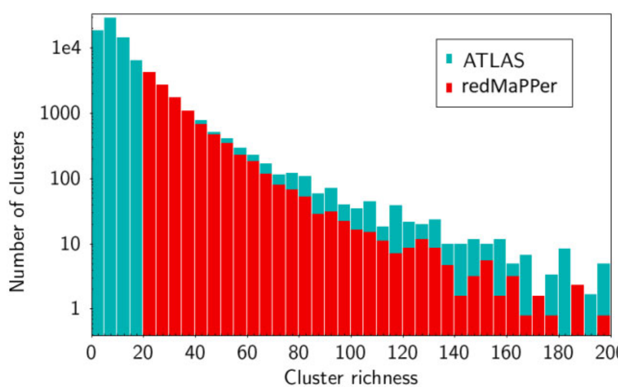

Figure 11. ATLAS cluster richness N_{200} distribution in comparison to SDSS redMaPPer cluster richness λ. Here both samples are limited to the redshift range $0.1 < z < 0.4$, and the redMaPPer histogram is scaled down by a factor of 2.2 to account for the differences between survey areas.

Figure 12. (a) Comparison of ATLAS, redMaPPer, and Abell clusters limited to the redshift range $0.05 < z < 0.35$ in the overlapping areas of ATLAS and SDSS. (b) Same as (a) but now ATLAS and redMaPPer are compared to ACT DR5 clusters with all samples limited to the redshift range $0.35 < z < 0.55$. In all cases, ATLAS, redMaPPer, and ACT clusters are limited to the $M_{200\mathrm{m}} > 3 \times 10^{14} h^{-1}\,\mathrm{M}_\odot$ mass range. We also note that the number density of Abell clusters in the ATLAS-SDSS overlap area in the NGC is ~ 50 per cent lower compared to the SGC.

the redshift range $0.05 < z < 0.35$ ATLAS appears to perform better than redMaPPer in recovering Abell and ACT DR5 clusters.[7] In the $0.35 < z < 0.55$ redshift range, however, redMaPPer appears to recover a larger fraction of ACT DR5 clusters than ATLAS. We also note that at higher redshifts there appears to be a larger number of redMaPPer clusters with no detections in ATLAS or ACT DR5 catalogues compared to lower redshift ATLAS clusters with no detections in the other catalogues.

Table 4 shows a comparison of the sky density of the ATLAS cluster catalogue to the SDSS redMaPPer catalogue in five bins of redshift ranging from $z = 0.05$–0.55. Similar to what we saw in Fig. 12, one can see here that in the redshift range $z < 0.35$ the ATLAS catalogue has a $\sim 3 \times$ higher cluster sky density compared to redMaPPer, while the two samples become more comparable at $z > 0.35$. A similar pattern can be seen in Fig. 13(b) where we compare the photometric redshift distributions of ATLAS and redMaPPer samples (without limiting the two samples to the survey overlap areas).

To further examine this, we calculate the detection rate of Abell clusters (which are classified as clusters with 30 or more members), by the redMaPPer catalogue across the full SDSS survey footprint. We find that redMaPPer only recovers ~ 60 per cent of the $0.05 <$

Table 4. Number and sky density (number of clusters per square degree) of ATLAS and SDSS redMaPPer cluster samples in different redshift bins. Here, the samples are limited to the overlap area of the two surveys and we apply a mass cut of $M_{200\mathrm{m}} > 3 \times 10^{14} h^{-1}\,\mathrm{M}_\odot$ to both samples.

	Number of clusters		Sky density	
Redshift	ATLAS	redMaPPer	ATLAS	redMaPPer
$0.05 < z < 0.15$	7	2	0.03	0.01
$0.15 < z < 0.25$	21	7	0.10	0.03
$0.25 < z < 0.35$	47	14	0.22	0.07
$0.35 < z < 0.45$	56	52	0.26	0.24
$0.45 < z < 0.55$	90	72	0.42	0.34

[7]We note that the Abell sample is not as complete as the ATLAS and redMaPPer samples as the latter surveys have the advantage of detecting clusters in multiple colours (with both catalogues detecting $\sim$3–4 times as many clusters as the Abell sample across their full survey footprints in the $z < 0.3$ redshift range). However, Abell is still a useful sample for comparison to ATLAS and redMaPPer, as clusters detected in both ATLAS and Abell samples are likely to be genuine rich clusters which should be detected by redMaPPer.

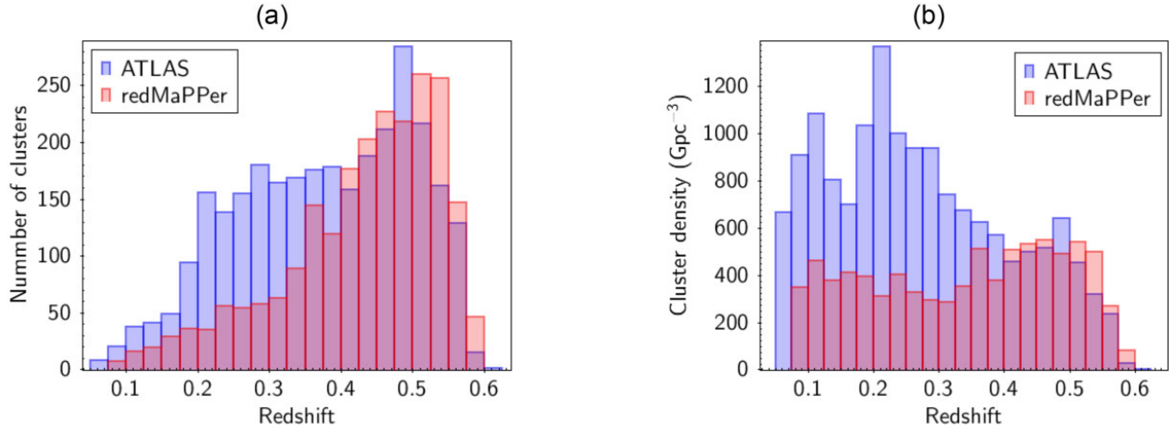

Figure 13. (a) A comparison of the photometric redshift distribution of full ATLAS and SDSS redMaPPer cluster catalogues. Here, both samples are restricted to clusters with $M_{200\mathrm{m}}>3\times10^{14}h^{-1}\,\mathrm{M}_\odot$. The redMaPPer histogram is scaled down by a factor of 2.2 to account for the difference between survey areas. (b) The number density of ATLAS and redMaPPer clusters per Gpc^3.

$z<0.3$ Abell clusters, compared to a ~85 per cent recovery rate in the ATLAS sample with a mass cut of $M_{200\mathrm{m}}>0.9\times10^{14}h^{-1}\,\mathrm{M}_\odot$ (which approximately corresponds to the lower mass limit of the redMaPPer sample given its $\lambda>20$ richness cut). Consequently, the higher number of ATLAS detections in this redshift range relative to redMaPPer is likely to be predominantly due to the incompleteness of the redMaPPer sample at lower redshifts.

We now explore the completeness and purity of the ATLAS sample as a function of redshift, based on direct comparison to redMaPPer in the $M_{200\mathrm{m}}>3\times10^{14}h^{-1}\,\mathrm{M}_\odot$ mass range. In column 2 of Table 5, for each redshift bin, we calculate the fraction of SDSS redMaPPer clusters (within the ATLAS coverage area) that are also detected by ORCA using the ATLAS data.[8] Here, our aim is to simply compute the likelihood that an SDSS redMaPPer cluster detection is also identified by ORCA in the ATLAS data. As such, when performing the matching, we only impose the mass and redshift cuts on the redMaPPer catalogue to allow for matches to be made in cases where the two catalogues assign the same cluster to different mass and redshift bins. These selections in effect ensure that our completeness estimates are not biased due to differences in photometric redshift and richness estimates between the two samples.

With these caveats in mind, we convert the recovery fractions shown in column (2) to percentages giving an estimate of the completeness of the ATLAS catalogue as a function of redshift (under the assumption that the redMaPPer sample is 100 per cent pure). Based on this comparison, we find that the ATLAS sample is 100 per cent complete up to $z<0.25$, with a slight reduction in completeness to 93 per cent between $0.25<z<0.35$ and a further reduction down to 63 per cent and 46 per cent completeness at $0.35<z<0.45$ and $0.45<z<0.55$, respectively. Although these values are presented here to show a full comparison of the two samples, we note that the mean completeness shown in Fig. 9(b) is likely to be a more reliable estimate of the completeness of the ATLAS cluster sample than estimates based on comparison to any one external sample alone.

In columns (4, 5, and 6) of Table 5, we estimate the purity of the ATLAS cluster catalogue based on comparison to the cluster detections by redMaPPer in the survey overlap region. As we are interested in assessing our sample purity as a function of redshift, we limit the ATLAS sample to photometric redshift bins shown in column (1) and look for confirmation that the ATLAS detection is also identified by redMaPPer. The fraction of ATLAS detections confirmed by redMaPPer in this way at each redshift bin is shown in column (4).

We note, however, that without access to the full redMaPPer catalogue we have no way of checking whether our clusters with no successful matches to redMaPPer may have been detected and classified by redMaPPer as clusters with $\lambda<20$, or indeed, remain undetected by redMaPPer. To overcome this limitation, in the next step we visually inspect the photometric redshifts of the clusters that were detected as $M_{200\mathrm{m}}>3\times10^{14}h^{-1}\,\mathrm{M}_\odot$ systems in ATLAS, but did not have a successful match in redMaPPer. We also count our cluster detections as 'pure' (i.e. non-spurious detections) if >50 per cent of the cluster members appear concentrated in a histogram with a width of $\bar{z}\pm0.025$ (corresponding to the ATLAS RMS error on cluster galaxy photometric redshifts). The choice of this criterion was motivated based on visual inspection of the photometric redshift histograms of ATLAS clusters with successful matches to redMaPPer, where almost all clusters detected in both catalogues had ATLAS or SDSS photometric redshift histograms which were centred around a redshift with more than half of cluster members lying within $\bar{z}\pm0.025$ of the histogram peak. Fig. 14 shows colour images and photometric redshift histograms of two $M_{200\mathrm{m}}>3\times10^{14}h^{-1}\,\mathrm{M}_\odot$ ATLAS clusters with no SDSS redMaPPer detections, which were confirmed as pure following the procedure described above.

The fraction of additional clusters confirmed as genuine cluster detections based on visual inspection is presented in column (5), with column (6) showing the sum of the fractions in columns (4 and 5) with the percentages in this column providing an estimate of the purity of the ATLAS cluster detections. Based on this estimate we find our $M_{200\mathrm{m}}>3\times10^{14}h^{-1}\,\mathrm{M}_\odot$ clusters to be 100 per cent pure at $z<0.25$, and 87 per cent pure in the redshift range $0.25<z<0.35$. The purity of the sample then falls to 71 per cent and 56 per cent in our final two redshift bins. This reduction of sample purity with increasing redshift could be partially due to the fact that as we reach the magnitude limits of the ATLAS and SDSS surveys the likelihood of real but faint cluster members not being detected by redMaPPer increases, bringing clusters with

[8] Similar to Section 4.3, we use the ORCA radius R_{ORCA} as our matching radius here and throughout the rest of this Section when comparing the two catalogues.

Table 5. Various comparisons of the intersections between the ATLAS and SDSS redMaPPer cluster catalogues. (columns 2 and 3) Fraction and percentage of SDSS redMaPPer clusters with detections in the ATLAS cluster catalogue. (4) The fraction of ATLAS clusters with counterpart detections in the redMaPPer catalogue. (5) Among the ATLAS clusters not matched to redMaPPer in column (4), how many clusters we constitute as genuine and rich detection clusters based on Visual Inspection (VI) of their photo-z $n(z)$. (6) The fraction of ATLAS detections that are either detected by redMaPPer or appear as likely detections based on the VI of the cluster $n(z)$s. (7) An estimate of the completeness of the redMaPPer based on the ratio of redMaPPer cluster detections to the number of 'pure' ATLAS detections (from column 6). We refer the reader to the discussion in the text for full details of the sample selections implemented prior to comparing the catalogues.

Redshift (1)	AT/RM (2)	AT Comp. (3)	RM/AT (4)	VI (5)	AT Purity (6)	RM Comp. (7)
$0.05 < z < 0.15$	2/2	100 per cent	5/7	+ 2/7	7/7 (100 per cent)	5/7 (71 per cent)
$0.15 < z < 0.25$	7/7	100 per cent	16/21	+ 6/21	21/21 (100 per cent)	16/21 (76 per cent)
$0.25 < z < 0.35$	13/14	93 per cent	29/47	+ 12/47	41/47 (87 per cent)	29/41 (70 per cent)
$0.35 < z < 0.45$	35/52	63 per cent	30/56	+ 10/56	40/56 (71 per cent)	30/40 (75 per cent)
$0.45 < z < 0.55$	33/72	46 per cent	23/90	+ 27/90	50/90 (56 per cent)	23/50 (46 per cent)

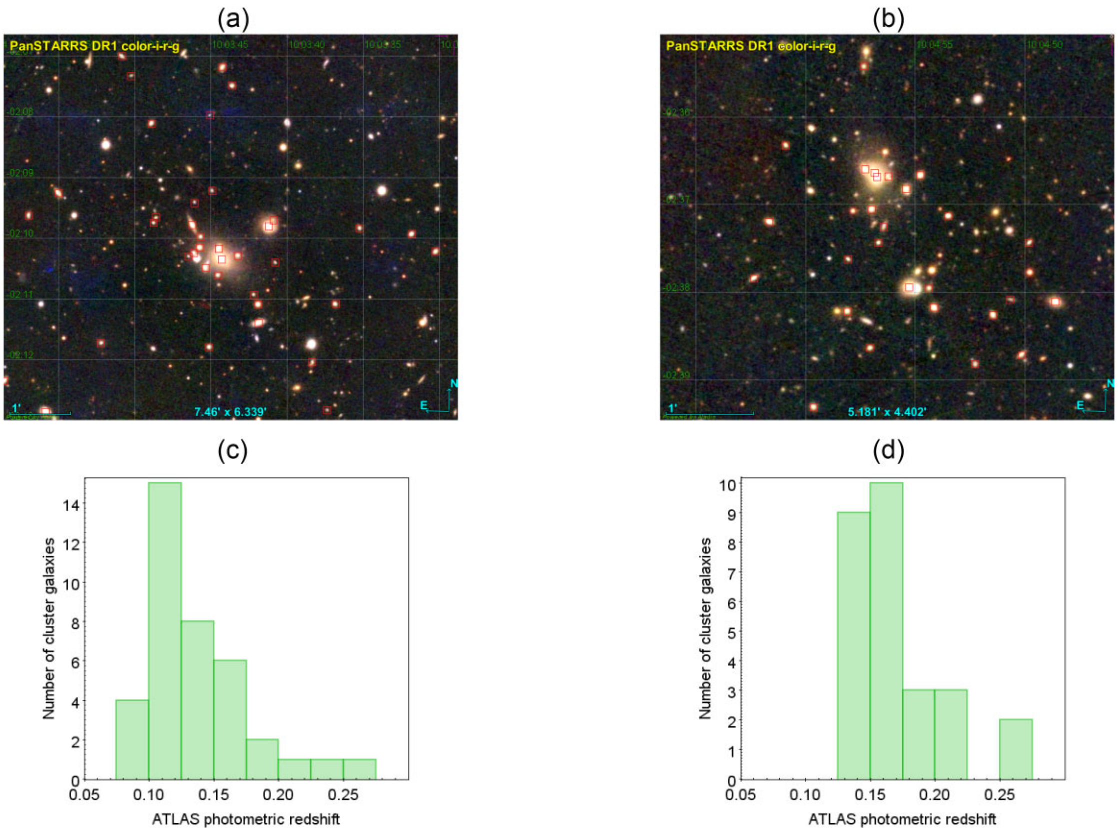

Figure 14. (a and b) PanSTARRS colour images of two $N_{200} > 20$ ATLAS clusters with no redMaPPer detections in SDSS. Here the cluster members identified in ORCA are shown by the red squares. (c and d) The photometric redshift histograms for clusters in panels (a and b), respectively.

richness greater than 20, below their $\lambda > 20$ limit. Similarly, the increase in the uncertainty on our estimated photometric redshifts with increasing redshift, reduces the number of clusters classified as pure on the basis of their photo-z histograms in column (5). On the other hand, it is also possible that at higher redshifts redMaPPer performs better than ORCA in overcoming projection effects which could artificially increase the richness of our clusters, or result in false cluster detections. We refer the reader to Section 6.4.3 of Murphy et al. (2012), for a different analysis of the purity of ORCA cluster detections as a function of cluster mass and redshift, based on comparison to SDSS-like simulated mock cluster catalogues. Based on this comparison, the purity of ORCA detections at the median redshift of the survey was shown to be > 70 per cent across all cluster masses.

Column (7) of Table 5 shows an estimate of the completeness of the redMaPPer sample, which is defined as the fraction of 'pure' ATLAS detections co-detected by redMaPPer.[9] We find the completeness of redMaPPer to be in the $\sim 70-75$ per cent range at $z < 0.45$, before falling down to ~ 50 per cent at $0.45 < z < 0.55$. At this point we remind the reader that although we were able to estimate the completeness of the ATLAS sample in

[9] We refer the reader to Section 11 of Rykoff et al. (2014) for a more systematic analysis of the completeness of the redMaPPer sample.

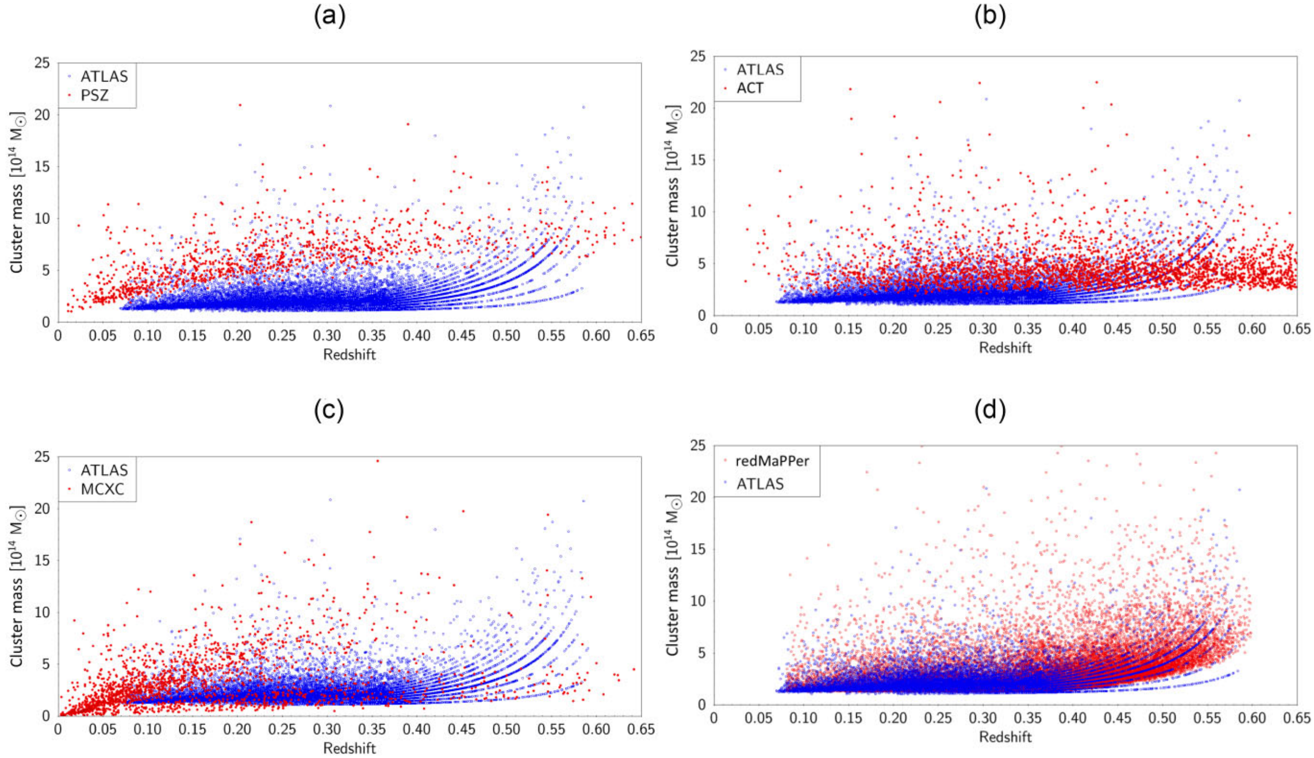

Figure 15. Comparison of the ATLAS $M_{200\mathrm{m}}$ cluster masses to Planck SZ masses M_{SZ} (panel a); ACT DR5 $M_{200\mathrm{m}}$ SZ masses (panel b); MCXC M_{500} cluster masses (panel c), and SDSS redMaPPer M_{200m} cluster masses (panel d).

column (3) by including successful matches between ATLAS and redMaPPer in cases where a $\lambda > 20$ redMaPPer cluster had an ATLAS detection with $N_{200} < 20$, we are unable to do the reverse in column 6. Here we recall that, while it is possible that some of our ATLAS detections may have redMaPPer counterparts with $\lambda < 20$ which would increase the redMaPPer completeness estimate; we have no way of verifying this. Indeed, this could explain the apparent fall in the completeness of the redMaPPer sample in the highest redshift bin where it is more likely for cluster richness to be underestimated due to the increased likelihood of cluster galaxies falling out of the survey magnitude limits. None the less, the information in column 7 provides a useful estimate of the percentage of low-redshift ATLAS clusters with $M_{200\mathrm{m}}>3\times10^{14}h^{-1}\,\mathrm{M}_\odot$ that are missed by redMaPPer, (possibly due to differences in our definitions of cluster richness and what constitutes a 'pure' cluster detection).

To summarize, comparison of the ATLAS cluster catalogue to redMaPPer shows that at $z < 0.35$ the ATLAS sample is highly complete, and the majority of our clusters appear to be genuine detections. At $z < 0.35$ we also find that a number of $M_{200\mathrm{m}}>3\times10^{14}h^{-1}\,\mathrm{M}_\odot$ ATLAS clusters (which were visually confirmed as rich clusters) are not detected as $\lambda > 20$ clusters by redMaPPer. Similarly, we found that ATLAS generally performs better than redMaPPer at recovering $z < 0.35$ Abell and ACT DR5 clusters, with ATLAS recovering ~ 85 per cent of $0.05 < z < 0.3$ Abell clusters while redMaPPer only recovers ~ 60 per cent of Abell clusters. At $z > 0.35$ while ATLAS appears to be less complete (65 per cent) compared to redMaPPer, Fig. 13(b) suggests that the additional redMaPPer cluster detections at higher redshifts tend to be clusters of lower mass with a good agreement being found between the $n(z)$ of the two samples for clusters with masses $M_{200\mathrm{m}}>3\times10^{14}h^{-1}\,\mathrm{M}_\odot$.

4.5 ATLAS cluster masses

Fig. 15 shows a comparison of the ATLAS cluster masses, obtained using equation (5), to SZ cluster masses of the full ACT DR5 and Planck samples. As seen in Fig. 15(a) the ATLAS cluster catalogue provides a complementary sample to the Planck catalogue, by detecting clusters in a lower mass range than possible with Planck. On the other hand, SZ cluster surveys offer the ability to detect all clusters above a certain mass threshold with little dependence on redshift, whereas optical surveys are limited in their ability to detect clusters at higher redshifts by the magnitude limit of the survey. As a result, the two approaches to cluster detection are highly complementary in maximizing the mass and redshift completeness of cluster samples.

As seen in Fig. 15(b), the ATLAS cluster sample also complements the ACT DR5 SZ sample in terms of detection of lower mass clusters in the redshift range $z < 0.5$. We note however, that due to it's higher angular resolution and superior flux sensitivity, ACT DR5 is able to detect lower mass SZ clusters than Planck. The larger Planck beam size, however, makes it more sensitive to clusters at $z < 0.05$ when compared to ACT DR5 (due to the larger projected area of these low redshift clusters on the sky).

Fig.15(c) shows a comparison of our ATLAS cluster masses, with X-ray cluster masses (M_{500}) from the MCXC sample. While most X-ray surveys included in the MCXC sample tend to be more sensitive to low-mass, low-redshift clusters in comparison to optical cluster catalogues, the completeness of these X-ray flux-limited cluster samples is reduced with redshift, with optical and SZ surveys providing more complete cluster samples at higher redshifts. Nevertheless, X-ray cluster samples play an important role in calibrating optical and SZ cluster masses and in determining the cluster gas fractions. The next generation of deeper X-ray cluster samples such as *eROSITA* will significantly improve on the completeness and statistics of current X-ray cluster samples by detecting ∼100 000 galaxy clusters with masses $> 5 \times 10^{13} h^{-1}$ M$_\odot$ (Pillepich, Porciani & Reiprich 2012), a 2 orders of magnitude improvement over the MCXC cluster sample size.

Finally, we compare the ATLAS cluster masses to cluster masses from the SDSS redMaPPer cluster catalogue in Fig. 15(d). It can be seen that the two samples cover a similar range of cluster masses and redshifts, which is expected, given that both samples detect clusters using optical *griz* bands with a similar depth. However, as the ATLAS catalogue covers areas of the southern sky, not covered by the SDSS redMaPPer catalogue, the two catalogues are highly complementary. For reasons which we discussed in Section 4.4, the ATLAS sample also contains a larger number of cluster detections in the redshift range $0.05 < z < 0.3$, while the redMaPPer catalogue contains more cluster detections in the $0.3 < z < 0.55$ range, making this another aspect in which the two catalogues are complementary.

4.6 Comparison of cluster mass functions

We now compare the observed cluster mass functions of ATLAS, redMaPPer, Planck, and ACT DR5 samples to the theoretical predictions of the Tinker et al. (2008) model. The mass function models are generated for spherical overdensities defined as M_{200m}, assuming the Planck 2015 cosmology (Planck Collaboration XIII 2016a; Table 4, column 6). We compare the observed mass functions to the models in five redshift bins, in order to examine the evolution of the cluster mass function in the redshift range $0.05 < z < 0.55$.

In Fig. 16 we compare the redshift evolution of observed optical and SZ cluster mass functions to the predictions of ΛCDM. For the purpose of visual comparison of the cluster mass functions, the error bars shown in this plot are simply estimated by $\sqrt{n}$, where n is the number of clusters in each mass bin. However, in Paper II, we shall perform a more detailed analysis of the mass function uncertainties prior to using the mass functions for cosmological parameter extraction. The fall in the amplitude of the cluster mass functions at lower masses seen in this figure is due to the reduced completeness of the samples as they approach their lower limit of cluster mass detection. As expected given the selection functions of ACT DR5 and Planck, the optical samples probe a lower range of cluster masses than the two SZ samples.

As seen in Fig. 16 in the $0.05 < z < 0.35$ redshift range, we find the ATLAS cluster mass functions to have a higher amplitude relative to redMaPPer, placing them in better agreement with the ΛCDM model predictions. Despite this closer agreement however, strong and unexplained tensions between the observed ATLAS mass functions and the model predictions are present, particularly at higher masses. The lower amplitude of redMaPPer could be in part due to an underestimation of redMaPPer cluster masses at lower redshifts. This is in line with the discussion presented in Section VI.B of Abbott et al. (2020), where the lower than expected $\Omega_{\rm m}$ obtained from cluster counts of the DES redMaPPer sample is attributed to a possible underestimation of the weak lensing estimated cluster masses for $\lambda < 30$ redMaPPer clusters.

However, in Section 4.4 we also found a higher density (per unit volume) of ATLAS clusters at $z < 0.35$ compared to redMaPPer. Similarly, our comparison of ATLAS and redMaPPer samples to the Abell cluster catalogue at lower redshifts showed that for clusters with $N_{200} > 20$, ATLAS recovers ∼ 85 per cent of Abell clusters, while redMaPPer recovers Abell clusters at a lower rate of ∼ 60 per cent. This could be taken as an indication that at lower redshifts redMaPPer is likely to miss a larger fraction of genuine (and relatively rich) clusters compared to ATLAS. Consequently, redMaPPer's lower completeness at $z < 0.35$ could also be an important contributing factor towards the lower amplitudes of its mass function relative to ΛCDM predictions.

As one can see in Fig. 16, although the ACT DR5 survey probes a lower range of cluster masses than Planck[10], at all redshifts we find a good agreement between the mass functions of the two SZ samples in the range of masses where both surveys are complete. With the exception of the $z = 0.5$ redshift bin (Fig. 16e), the Planck and ACT DR5 mass functions also appear to be in general agreement with redMaPPer, placing them below the ATLAS cluster mass functions and the predictions of ΛCDM.

The lower amplitude of the SZ cluster mass functions compared to ΛCDM is likely to be due to systematics in the SZ flux-cluster mass scaling relation resulting in an underestimation of cluster masses of these samples. Indeed, some SZ mass calibration techniques place the Planck cluster counts in closer agreement to the prediction of the ΛCDM model. However, the incompleteness of SZ samples could be another explanation for the lower amplitude of their mass functions relative to the models. To investigate this possibility, we compare the ACT DR5[11] and Planck samples to the Abell clusters with richness classes >2 and >3 (which limit the catalogue to clusters with greater than 80 and 130 members, respectively). A summary of our results is presented in Table 6, where we find the SZ samples to recover ∼ 30 per cent of Abell clusters with a richness class > 2 and ∼ 50 per cent of Abell clusters with richness > 3. Fig. 17 shows examples of four $z \sim 0.2$ ATLAS clusters with mass estimates of $M_{\rm 200m} > 4 \times 10^{14} h^{-1}$ M$_\odot$ placing them above the Planck lower limit on mass observability. In the future, spectroscopic follow up of SZ clusters guided by optical cluster catalogues could improve the completeness of current SZ samples. Similarly, a more detailed study of potential issues which could lead to the lack of detection of rich clusters in SZ samples based on comparison to optical catalogues such as ATLAS and redMaPPer would be an interesting topic for future works.

Although the lower amplitude of SZ cluster mass functions relative to the ΛCDM predictions could be due to the issues described above, we note that a value of $\sigma_8 \approx 0.7$ (with $\Omega_{\rm m} = 0.3$), could also produce such observations. Furthermore, suppression of observed cluster mass functions compared to ΛCDM predictions at higher masses (similar to those seen in the ATLAS mass functions) could originate from primordial non-Gaussianities (Dalal et al. 2008; Verde 2010) or signal the presence of massive neutrinos (e.g. Costanzi et al. 2013; Castorina et al. 2014; Biswas et al. 2019).

While this comparison provides a preliminary indication of the divergence of observations to predictions of the model, a more comprehensive analysis of the systematic and statistical uncertainties on the ATLAS cluster mass function is needed before the statistical significance of the divergence between the observations and the predictions can be quantified. We leave this, as well as comparison of the observations to different mass function models, and obtaining constraints on various cosmological parameters from the ATLAS cluster mass functions to Paper II in this series.

[10]Note that in the $z = 0.1$ bin (Fig. 16a) the fact that Planck probes lower redshifts than ACT DR5, offsets ACT DR5's ability to probe clusters of lower masses, resulting in both samples having a similar completeness in the $M_{\rm 200m} < 3 \times 10^{14} h^{-1}$ M$_\odot$ mass range.

[11]We note that although Planck SZ detections with no measured redshifts are included in the catalogue used in this comparison, at the time of this writing, we only had access to ACT DR5 SZ detections with cluster counterparts identified based on their photometric or spectroscopic redshifts.

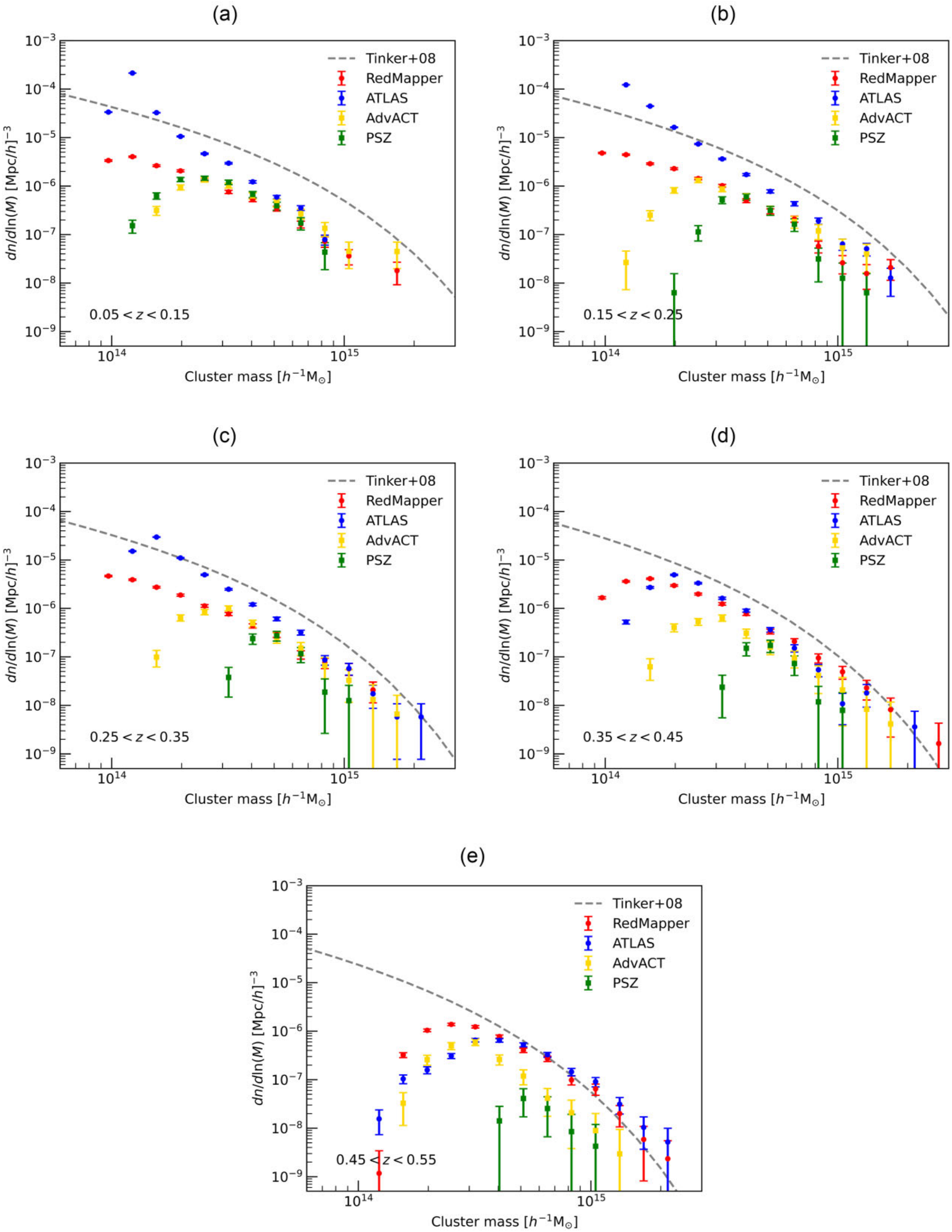

Figure 16. A comparison of ATLAS, redMaPPer, Planck, and ACT DR5 cluster mass functions to the theoretical predictions of the Tinker et al. (2008) ΛCDM models assuming a Planck Collaboration XIII (2016a) cosmology. Here, the error bars on the observed mass functions are simply estimated as $\sqrt{n}$.

5 CONCLUSIONS

In this work, we have presented a new catalogue of photometrically detected galaxy groups and clusters, using the ORCA cluster detection algorithm in combination with the *griz* bands of the VST ATLAS survey, covering ∼4700 deg^2 of the Southern sky. The catalogue contains ∼22 000 detections with richness N_{200} > 10 and ∼9000

Table 6. Fraction/percentage of rich Abell clusters overlapping the Planck and ACT DR5 surveys recovered by each SZ survey. ACO2 and ACO3 denote Abell clusters with richness class > 2 and 3, respectively.

Redshift	ACT DR5/ACO2	PSZ/ACO2	ACT DR5/ACO3	PSZ/ACO3
$0.05 < z < 0.15$	16/73 (22 per cent)	50/170 (29 per cent)	4/9 (44 per cent)	13/29 (65 per cent)
$0.15 < z < 0.25$	34/105 (32 per cent)	105/300 (35 per cent)	13/28 (46 per cent)	36/64 (56 per cent)

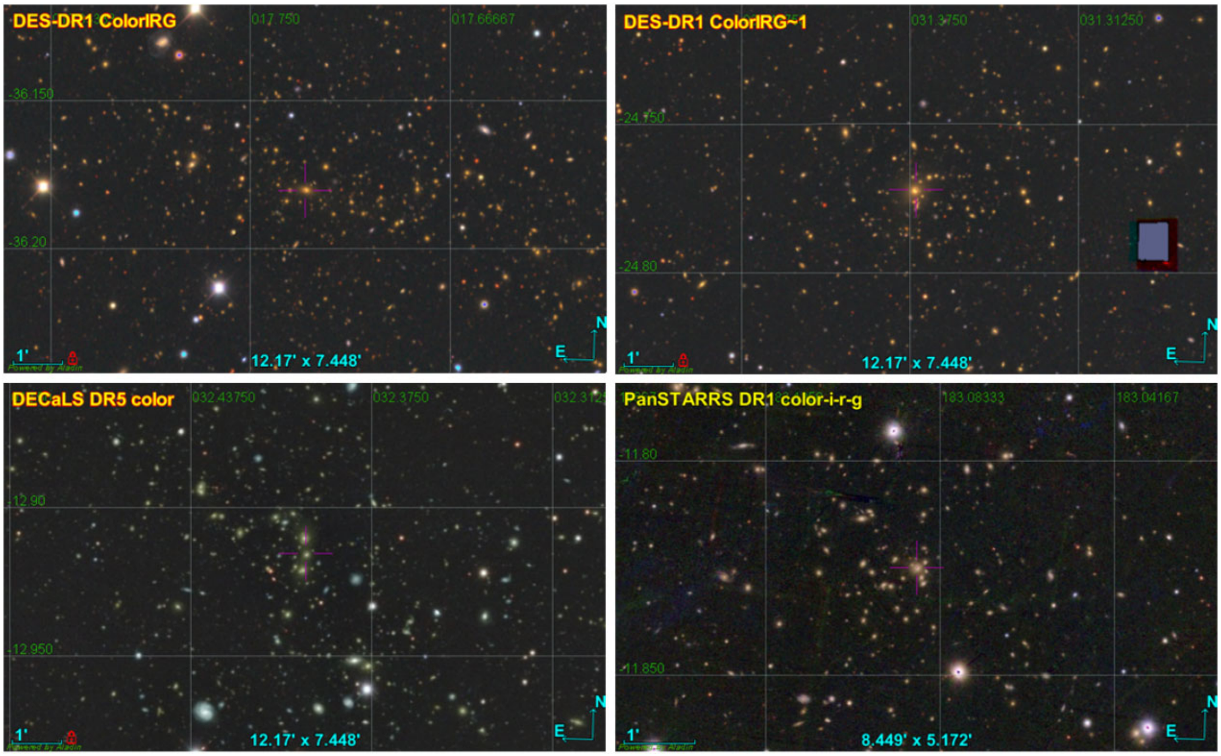

Figure 17. DES, DECaLS, or PanSTARRS images of four $z \sim 0.2$, $M_{200\mathrm{m}}>4 \times 10^{14} h^{-1}\,\mathrm{M}_{\odot}$ ATLAS clusters which are also detected in the Abell sample, with no detections in the Planck SZ catalogue.

clusters with $N_{200} > 20$. Using the ANNZ2 machine learning algorithm we obtain photometric redshift estimates with an RMS of $\sim$0.025 for our cluster galaxies and a mean redshift uncertainty of $\sim$0.01 for our clusters with richness $N_{200} > 20$. The photometric redshift of our sample peaks at $z \sim 0.25$, extending up to $z = 0.7$.

We described our calculation of cluster richness (N_{200}) which we use as a proxy for cluster mass ($M_{200\mathrm{m}}$). To this end, we calibrated the mass-richness scaling relation of the ATLAS sample to cluster masses from the SDSS redMaPPer, MCXC, Planck, and ACT DR5 samples. We found the ATLAS sample to be > 95 per cent complete at $z < 0.35$, > 80 per cent complete up to $z = 0.45$, and ~ 60 per cent complete in the $0.45 < z < 0.65$ redshift range. In terms of cluster mass, we found the sample to be greater than ~ 95 per cent complete for all cluster masses, with near full completeness in the $> 5 \times 10^{14} h^{-1}\,\mathrm{M}_{\odot}$ mass range. Based on a comparison to the SDSS redMaPPer cluster detections as well as visual inspection of our clusters, we estimate the purity of our cluster detections with $M_{200\mathrm{m}}>3 \times 10^{14} h^{-1}\,\mathrm{M}_{\odot}$ to be 100 per cent in the range $z < 0.25$, 87 per cent at $0.25 < z < 0.35$, 71 per cent at $0.35 < z < 0.45$ and 56 per cent at $0.45 < z < 0.55$.

Our comparison to the redMaPPer catalogue showed that in the $0.05 < z < 0.35$ redshift range, the ATLAS sample contains a larger number of cluster detections and recovers an ~ 40 per cent higher fraction of Abell clusters compared to redMaPPer. At higher redshifts ($0.35 < z < 0.55$) the redMaPPer catalogue appears to perform better than ATLAS at recovering ACT DR5 clusters, but also detects a large number of clusters not found in the ACT DR5 sample which could be lower mass groups which are misclassified as $\lambda > 20$ clusters. At $z > 0.35$ we also find a good agreement between the redshift distributions of the ATLAS and redMaPPer samples above a mass limit of $M_{200\mathrm{m}}>3 \times 10^{14} h^{-1}\,\mathrm{M}_{\odot}$.

We then compared the cluster mass functions of ATLAS, redMaPPer, Planck, and ACT DR5 samples to the theoretical predictions of Tinker et al. (2008) models (assuming a Planck Collaboration XIII 2016a ΛCDM cosmology), in the $0.05 < z < 0.55$ redshift range. At $z < 0.35$, ATLAS cluster mass functions have a higher amplitude compared to those of the SZ samples and the redMaPPer mass functions. This places the ATLAS measurements in better agreement with ΛCDM predictions with $\sigma_8 \approx 0.82 \pm 0.01$ (based on the CMB analysis of Planck Collaboration XIII 2016a), rather than some of the previous constraints from the Planck SZ cluster counts, which depending on the SZ mass calibrations, can give σ_8 measurements as low as 0.71 ± 0.03 (Planck Collaboration XIII 2016b). Despite this closer agreement, however, at higher masses we found the observed

ATLAS mass functions to have a significantly lower amplitude than the ΛCDM model and the cause of this discrepancy is currently unknown.

Based on our earlier findings, we suggest that the incompleteness of the SDSS redMaPPer sample at lower redshifts could be a contributing factor to the lower amplitude of its mass functions relative to the predictions of ΛCDM. For the SZ samples, while mass calibration systematics are likely to be the dominant contributing factor to their lower mass function amplitudes relative to ΛCDM predictions, we show that sample incompleteness is also likely to have a non-negligible contribution and will need to be carefully characterized and accounted for. Future follow-up spectroscopic observations of SZ clusters guided by optical cluster catalogues such as ATLAS and redMaPPer could improve the completeness of SZ samples, while detailed studies of rich optical clusters which remain undetected in SZ samples could help with the identification of any unknown issues impacting the completeness of SZ catalogues.

In paper II of this series, we shall perform a detailed analysis of the systematic and statistical uncertainties of the ATLAS cluster mass functions. This will in turn enable us to constrain various cosmological parameters including, σ_8, Ω_m, ω, and $\sum m_\nu$ and compare these to constraints from other cluster samples and different cosmological probes.

ACKNOWLEDGEMENTS

BA acknowledges support from the Australian Research Council's Discovery Projects scheme (DP200101068). This work used the Distributed Research Utilising Advanced Computing DiRAC@Durham facility managed by the Institute for Computational Cosmology on behalf of the Science and Technology Facilities Council (STFC) DiRAC HPC Facility (www.dirac.ac.uk). The equipment was funded by BEIS capital funding via STFC capital grants ST/K00042X/1, ST/P002293/1, ST/R002371/1, and ST/S002502/1, Durham University and STFC operations grant ST/R000832/1. DiRAC is part of the National e-Infrastructure. For the purpose of open access, the author has applied a Creative Commons Attribution (CC BY) licence to any Author Accepted Manuscript version arising. TS and NM acknowledge STFC support from ST/T000244/1.

The mass function models in Fig. 16 are generated using the 'Halo mass function' module of the COLOSSUS python package described by Diemer (2018). This research has made extensive use of Python 2 & 3 (Van Rossum & Drake 1995; Van Rossum & Drake 2009), IPYTHON (Perez & Granger 2007), MATPLOTLIB (Hunter 2007), SCIPY (Virtanen et al. 2020), NUMPY (van der Walt, Colbert & Varoquaux 2011), PANDAS (Wes McKinney 2010), ASTROPY (Price-Whelan et al. 2018), as well as TOPCAT & STILTS[12] packages (Taylor 2005). This research has made use of the NASA/IPAC Extragalactic Database, which is funded by the National Aeronautics and Space Administration and operated by the California Institute of Technology, as well as the 'Aladin sky atlas' developed at CDS, Strasbourg Observatory, France.

This publication makes use of data products from the Wide-field Infrared Survey Explorer, which is a joint project of the University of California, Los Angeles, and the Jet Propulsion Laboratory/California Institute of Technology, funded by the National Aeronautics and Space Administration. Funding for the Sloan Digital Sky Survey IV has been provided by the Alfred P. Sloan Foundation, the U.S. Department of Energy Office of Science, and the Participating Institutions. SDSS-IV acknowledges support and resources from the Center for High-Performance Computing at the University of Utah. The SDSS web site is www.sdss.org. The Pan-STARRS1 Surveys (PS1) and the PS1 public science archive have been made possible through contributions by the Institute for Astronomy, the University of Hawaii, the Pan-STARRS Project Office, the Max-Planck Society and its participating institutes, the Max Planck Institute for Astronomy, Heidelberg and the Max Planck Institute for Extraterrestrial Physics, Garching, The Johns Hopkins University, Durham University, the University of Edinburgh, the Queen's University Belfast, the Harvard-Smithsonian Center for Astrophysics, the Las Cumbres Observatory Global Telescope Network Incorporated, the National Central University of Taiwan, the Space Telescope Science Institute, the National Aeronautics and Space Administration under Grant No. NNX08AR22G issued through the Planetary Science Division of the NASA Science Mission Directorate, the National Science Foundation Grant No. AST-1238877, the University of Maryland, Eotvos Lorand University (ELTE), the Los Alamos National Laboratory, and the Gordon and Betty Moore Foundation. This publication makes use of data products from the Wide-field Infrared Survey Explorer, which is a joint project of the University of California, Los Angeles, and the Jet Propulsion Laboratory/California Institute of Technology, funded by the National Aeronautics and Space Administration.

[12]http://www.star.bris.ac.uk/ mbt/topcat/sun253/index.html

DATA AVAILABILITY

The cluster catalogues described in Tables 2 and 3 are publicly available at http://astro.dur.ac.uk/cosmology/vstatlas/cluster_catalogue/. The input galaxy catalogues used for cluster detection are also available from the primary author upon request.

REFERENCES

Abbott T. M. C. et al., 2020, Phys. Rev. D, 102, 023509
Aihara H. et al., 2018, PASJ, 70, S8
Alam S. et al., 2015, ApJS, 219, 12
Allen S. W., Schmidt R. W., Fabian A. C., 2002, MNRAS, 334, L11
Allen S. W., Evrard A. E., Mantz A. B., 2011, ARA&A, 49, 409
Baum W. A., 1959, PASP, 71, 106
Benítez N., 2011, BPZ: Bayesian Photometric Redshift Code, Astrophysics Source Code Library, record ascl:1108.011
Bertin E., Arnouts S., 1996, A&AS, 117, 393
Biswas R., Heitmann K., Habib S., Upadhye A., Pope A., Frontiere N., 2019, preprint (arXiv:1901.10690)
Bleem L. E. et al., 2015, ApJS, 216, 27
Bocquet S. et al., 2019, ApJ, 878, 55
Bolzonella M., Miralles J.-M., Pelló R., 2000, A&A, 363, 476
Bower R. G., Lucey J. R., Ellis R. S., 1992, MNRAS, 254, 589
Brownstein J. R., 2009, PhD thesis, University of Waterloo, Canada
Bruzual G., Charlot S., 2003, MNRAS, 344, 1000
Carlstrom J. E., Holder G. P., Reese E. D., 2002, ARA&A, 40, 643
Carlstrom J. E. et al., 2011, PASP, 123, 568
Castorina E., Sefusatti E., Sheth R. K., Villaescusa-Navarro F., Viel M., 2014, J. Cosmol. Astropart. Phys., 2014, 049
Cavaliere A., Fusco-Femiano R., 1976, A&A, 49, 137
Chilingarian I. V., Melchior A.-L., Zolotukhin I. Y., 2010, MNRAS, 405, L11
Colless M. et al., 2003, preprint (arXiv:astro-ph/0306581)
Cool R. J. et al., 2013, ApJ, 767, 118
Costanzi M., Villaescusa-Navarro F., Viel M., Xia J.-Q., Borgani S., Castorina E., Sefusatti E., 2013, J. Cosmol. Astropart. Phys., 2013, 012
DESI Collaboration 2016, preprint (arXiv:1611.00036)
Dalal N., Doré O., Huterer D., Shirokov A., 2008, Phys. Rev. D, 77, 123514
Dawson K. S. et al., 2013, AJ, 145, 10
de Jong J. T. A. et al., 2013, The Messenger, 154, 44

de Jong R. S. et al., 2019, The Messenger, 175, 3
Diemer B., 2018, ApJS, 239, 35
Ebeling H. et al., 2013, MNRAS, 432, 62
Evrard A. E., 1997, MNRAS, 292, 289
Fowler J. W. et al., 2007, Appl. Opt., 46, 3444
Girardi M., Manzato P., Mezzetti M., Giuricin G., Limboz F., 2002, ApJ, 569, 720
Gladders M. D., Yee H. K. C., 2000, AJ, 120, 2148
Gladders M. D., Yee H. K. C., Majumdar S., Barrientos L. F., Hoekstra H., Hall P. B., Infante L., 2007, ApJ, 655, 128
González-Solares E. A. et al., 2008, MNRAS, 388, 89
Hansen S. M., McKay T. A., Wechsler R. H., Annis J., Sheldon E. S., Kimball A., 2005, ApJ, 633, 122
Hao J. et al., 2010, ApJS, 191, 254
Hasselfield M. et al., 2013, J. Cosmol. Astropart. Phys., 2013, 008
Hilton M. et al., 2021, ApJS, 253, 3
Høg E. et al., 2000, A&A, 355, L27
Hunter J. D., 2007, Comput. Sci. Eng., 9, 90
Kaiser N. et al., 2002, in Tyson J. A., Wolff S.eds, Proc. SPIE Conf. Ser. Vol. 4836, Survey and Other Telescope Technologies and Discoveries. SPIE, Bellingham, p. 154
Koester B. P. et al., 2007, ApJ, 660, 239
Kravtsov A. V., Borgani S., 2012, ARA&A, 50, 353
LSST Dark Energy Science Collaboration, 2012, preprint (arXiv:1211.0310)
Laureijs R. et al., 2011, preprint (arXiv:1110.3193)
Lin Y.-T., Mohr J. J., Stanford S. A., 2003, ApJ, 591, 749
Lin Y.-T., Mohr J. J., Gonzalez A. H., Stanford S. A., 2006, ApJ, 650, L99
Liske J. et al., 2015, MNRAS, 452, 2087
Llinares C., Mota D. F., 2013, Phys. Rev. Lett., 110, 151104
Loveday J. et al., 2012, MNRAS, 420, 1239
Menanteau F. et al., 2010, ApJ, 723, 1523
Merloni A. et al., 2012, preprint (arXiv:1209.3114)
Morandi A., Sun M., 2016, MNRAS, 457, 3266
Murphy D. N. A., Geach J. E., Bower R. G., 2012, MNRAS, 420, 1861
Muzzin A., Yee H. K. C., Hall P. B., Lin H., 2007, ApJ, 663, 150
Peebles P. J. E., 1980, The Large-Scale Structure of the Universe. Princeton University Press, Princeton, NJ
Perez F., Granger B. E., 2007, Comput. Sci. Eng., 9, 21
Piffaretti R., Arnaud M., Pratt G. W., Pointecouteau E., Melin J.-B., 2011, A&A, 534, A109
Pillepich A., Porciani C., Reiprich T. H., 2012, MNRAS, 422, 44
Planck Collaboration VIII, 2011, A&A, 536, A8
Planck Collaboration XVI, 2014a, A&A, 571, A11
Planck Collaboration XVI, 2014b, A&A, 571, A29
Planck Collaboration XIII, 2016a, A&A, 594, A13
Planck Collaboration XIII, 2016b, A&A, 594, A24
Planck Collaboration XIII, 2016c, A&A, 594, A27
Popesso P., Biviano A., Böhringer H., Romaniello M., 2007, A&A, 464, 451
Price-Whelan A. M. et al., 2018, AJ, 156, 18
Radovich M. et al., 2017, A&A, 598, A107
Reichardt C. L. et al., 2013, ApJ, 763, 127
Reyes R., Mandelbaum R., Hirata C., Bahcall N., Seljak U., 2008, MNRAS, 390, 1157
Rines K., Geller M. J., Diaferio A., Kurtz M. J., Jarrett T. H., 2004, AJ, 128, 1078
Roncarelli M., Carbone C., Moscardini L., 2015, MNRAS, 447, 1761
Rosati P., Borgani S., Norman C., 2002, ARA&A, 40, 539
Rykoff E. S. et al., 2014, ApJ, 785, 104
Rykoff E. S. et al., 2016, ApJS, 224, 1
Sadeh I., Abdalla F. B., Lahav O., 2016, PASP, 128, 104502
Schechter P., 1976, ApJ, 203, 297
Schipani P. et al., 2012, Proc. SPIE Conf. Ser. Vol. 8444, Ground-based and Airborne Telescopes IV. SPIE, Bellingham, p. 84441C
Schlafly E. F., Meisner A. M., Green G. M., 2019, ApJS, 240, 30
Schneider D. P. et al., 2007, AJ, 134, 102
Schuecker P., Caldwell R. R., Böhringer H., Collins C. A., Guzzo L., Weinberg N. N., 2003, A&A, 402, 53
Shanks T. et al., 2015, MNRAS, 451, 4238
Simet M., McClintock T., Mandelbaum R., Rozo E., Rykoff E., Sheldon E., Wechsler R. H., 2016, MNRAS, 466, 3103
Soucail G., Foëx G., Pointecouteau E., Arnaud M., Limousin M., 2015, A&A, 581, A31
Sunyaev R. A., Zeldovich I. B., 1980, ARA&A, 18, 537
Tauber J. A. et al., 2010, A&A, 520, A1
Taylor M. B., 2005, in Shopbell P., Britton M., Ebert R.eds, ASP Conf. Ser. Vol. 347, Astronomical Data Analysis Software and Systems XIV. Astron. Soc. Pac., San Francisco, p. 29
Taylor M. B., 2006, in Gabriel C., Arviset C., Ponz D., Enrique S., eds, ASP Conf. Ser. Vol. 351, Astronomical Data Analysis Software and Systems XV. Astron. Soc. Pac., San Francisco, p. 666
Thanjavur K., Willis J., Crampton D., 2009, ApJ, 706, 571
The Dark Energy Survey Collaboration, 2005, preprint (arXiv:astro-ph/0510346)
Tinker J., Kravtsov A. V., Klypin A., Abazajian K., Warren M., Yepes G., Gottlöber S., Holz D. E., 2008, ApJ, 688, 709
Van Rossum G., Drake F. L., 2009, Python 3 Reference Manual. CreateSpace, Scotts Valley, CA
Van Rossum G., Drake F. L. Jr, 1995, Python Reference Manual. Centrum voor Wiskunde en Informatica, Amsterdam
Vanderlinde K. et al., 2010, ApJ, 722, 1180
Verde L., 2010, Adv. Astron., 2010, 768675
Vikhlinin A. et al., 2009, ApJ, 692, 1060
Virtanen P. et al., 2020, Nat. Methods, 17, 261
Voit G. M., 2005, Rev. Mod. Phys., 77, 207
Weinberg D. H., Mortonson M. J., Eisenstein D. J., Hirata C., Riess A. G., Rozo E., 2013, Phys. Rep., 530, 87
McKinney , 2010, in van der Walt S., Millman J., eds, Proc. of the 9th Python in Science Conf. 56 (SCIPY 2010) Data Structures for Statistical Computing in Python. SciPy, Austin Texas, p. 56
White S. D. M., Efstathiou G., Frenk C. S., 1993, MNRAS, 262, 1023
Wolf C. et al., 2017, MNRAS, 466, 1582
York D. G. et al., 2000, AJ, 120, 1579
Yuan H. B., Liu X. W., Xiang M. S., 2013, MNRAS, 430, 2188
van der Walt S., Colbert S. C., Varoquaux G., 2011, Comput. Sci. Eng., 13, 22

SUPPORTING INFORMATION

Supplementary data are available at *MNRAS* online.

suppl_data

Please note: Oxford University Press is not responsible for the content or functionality of any supporting materials supplied by the authors. Any queries (other than missing material) should be directed to the corresponding author for the article.

This paper has been typeset from a TEX/LATEX file prepared by the author.